Clays and Clay Minerals, Vol. 66, No. 2, 146–172, 2018.

OCCURRENCE OF FIBROUS CHRYSOTILE AND TREMOLITE IN THE ÇANKIRI AND ANKARA REGIONS, CENTRAL ANATOLIA, TURKEY

TACİT KÜLAH[1], SELAHATTİN KADİR[2,*], HÜLYA ERKOYUN[2], JENNIFER HUGGETT[3], AND EŞREF ATABEY[4]

[1] Kütahya Dumlupınar University, Department of Geological Engineering, TR-43100 Kütahya, Turkey
[2] Eskişehir Osmangazi University, Department of Geological Engineering, TR-26480 Eskişehir, Turkey
[3] Natural History Museum, Department of Earth Sciences, London, UK
[4] Hacettepe University, Mesothelioma and Medical Geology Research Center, Ankara, Turkey

Abstract—Numerous occurrences of asbestos minerals, notably chrysotile and tremolite, are to be found on fracture surfaces in thrust fault deformation zones of Cretaceous dunite-harzburgite and pyroxenite in the Çankırı and Ankara regions, central Anatolia, Turkey. Consequently, potential exists for the development of regional malignant mesothelioma. The means of serpentinization, such as reaction of seawater during accretion of the upper ophiolitic mantle crust in a subduction zone and/or following uplift of ophiolitic units and the influence of hydrothermal/meteoric fluids along fractures, were investigated. Cretaceous dunite-harzburgite and localized pyroxenite rocks are mainly composed of serpentinized olivine and pyroxene associated with opaque minerals and Fe-(oxyhydr)oxide phases. Smectite, chlorite, illite, kaolinite, hydromagnesite, goethite, quartz, and opal-CT are also present. Chrysotile and localized tremolite occur either as a mesh, a suboriented to oriented long-fiber bundle, or as fiber-filling millimetric micro-vein textures on relicts of olivine and pyroxene (enstatite, augite). The chrysotile and tremolite have non-pseudomorphic textures developed under high pressure and temperature. The textures suggest authigenic formation of chrysotile and tremolite *via* a dissolution and precipitation mechanism. Additionally, spherical structures of opal-CT and locally platy hydromagnesite crystals either enclose or are developed within chrysotile/tremolite fiber bundles. The leaching of MgO, Fe_2O_3, Al_2O_3, Ni, Cr, and Nb, an increase in the *LREE*/*HREE* ratio, and negative Eu anomalies in the dunite-harzburgite and pyroxenite, and asbestos samples suggest that the chrysotile and tremolite were derived from the serpentinization of olivine and pyroxene. The chrysotile and tremolite were developed along fractures by hydrothermal fluid alteration during accretion and/or following the uplift of ophiolitic units of the region under high pressure and temperature conditions. This interpretation is also supported by isotope data and the calculated formation temperature of 170−555ºC for chrysotile and tremolite. The average structural formulae for chrysotile and tremolite are $(Na_{0.44}K_{0.03})(Mg_{5.54}Fe_{0.09}Al_{0.05}Ca_{0.01}Mn_{0.001})(Si_{3.96}Al_{0.03})O_{10}(OH)_8$ and $(Na_{0.17}K_{0.07})(Ca_{1.59}Mg_{0.19}Mn_{0.002})(Mg_{4.72}Fe_{0.28})(Si_{7.86}Al_{0.1}Fe_{0.06})O_{22}(OH)_2$, respectively.

Key Words—Ankara, Çankırı, Chrysotile, Genesis, Mesothelioma, Tremolite, Turkey.

INTRODUCTION

The serpentinization process has been studied in depth by many researchers in the past few decades (*e.g.* Moody, 1976; O'Hanley, 1996; Mével, 2003; Niu, 2004; Khedr and Arai, 2009; Pacella *et al.*, 2010; Barnes *et al.*, 2013; Biondi, 2014; Lamadrid *et al.* 2017). Serpentinization occurs in various geological settings: (1) in relation to magmatism and extension along mid-ocean ridges at the slow-spreading of divergent margins; (2) by reaction of dunite and harzburgite from the sub-arc mantle with fluids at nonaccretionary convergent margins; (3) by thrusting of the forearc mantle over the accretionary wedge in a forearc setting or thrusting over the passive margin or the arc in a back-arc setting of ophiolites; and (4) by reaction of seawater or a hydrothermal fluid with ultramafic rocks in greenstone belts (Iyer, 2007 and references therein). In these settings, the influence of hydrothermal fluids in addition to seawater and groundwater have a very important role.

Wicks and Whittaker (1977) also classified the formation conditions of serpentine minerals in different geological environments based on their pseudomorphic or non-pseudomorphic textural properties and mineral paragenesis. According to this classification scheme, serpentinization develops under a variety of temperature, shear, and mineral nucleation regimes.

Asbestos minerals, such as chrysotile and tremolite, are abundant in the widespread, altered ophiolitic rock patterns of Anatolia (Kadir and Erkoyun, 2015). Ophiolitic rocks of the study area are part of the İzmir-Ankara-Erzincan Suture Zone (IAESZ). The geology of the study area has been previously examined for various reasons, including the stratigraphy, geochronology, petrology (Hakyemez *et al.*, 1986; Dilek and Thy, 2006; Gökten and Floyd, 2007; Sarıfakıoğlu *et al.*, 2011, 2014, 2017), and tectonics (Koçyiğit, 1987; Koçyiğit *et al.*, 1995; Okay and Tüysüz, 1999;

* E-mail address of corresponding author:
skadir.euroclay@gmail.com
DOI: 10.1346/CCMN.2018.064088

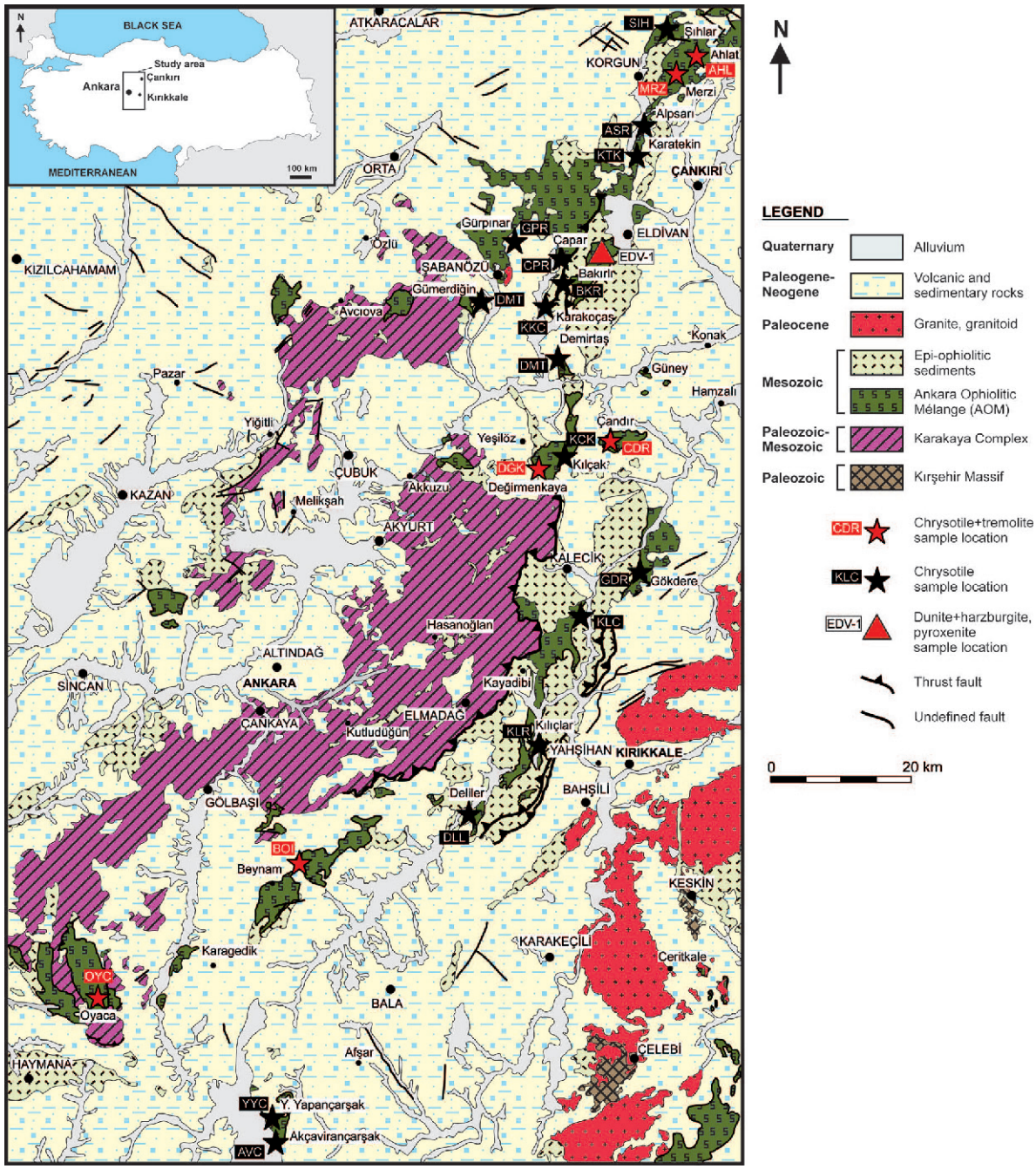

Figure 1. Geological map of the Çankırı and Ankara regions (modified from MTA, 2002).

Kaymakçı, 2000; Dangerfield *et al*., 2011; Rojay, 2013). Üner and Çakır (2011) studied the mineralogy, petrography, and geochemistry of dunite, harzburgite, and pyroxenite in an ophiolitic mélange. Çelik *et al*. (2011) determined the genesis of amphibole levels within an ophiolitic mélange based on the rare earth element contents. Atabey (2009) determined the geological distribution of erionite, quartz, chrysotile, antigorite, and lizardite in central Anatolia. Atabey (2009) also published a map of asbestos distribution in the regions and their occurrence in the study area. The asbestos materials are used for wall insulation and to waterproof floors and roofs in Çapar and Karakoçaş villages (Atabey, 2009, 2015; Atabey and Ünal, 2008).

The close relationship between mesothelioma cases and the occurrence of asbestos materials is well known in Turkey and worldwide (Barış, 1987, 1994; Metintaş *et al*., 1999; Metintas *et al*., 2002a, 2002b; Ross and Nolan,

https://doi.org/10.1346/CCMN.2018.064088 Published online by Cambridge University Press

2003; Metintas *et al*., 2008; Atabey, 2009; Foresti *et al*., 2009; Döngel *et al*., 2013; Bayram *et al*., 2013; Lescano *et al*., 2015; Turkish Mesothelioma Working Group, 2015). Metintaş *et al.* (2017) reported that environmental asbestos fiber exposure is a serious health risk and leads to the development of malignant mesothelioma worldwide and in the rural regions of Anatolia. From the XRD analyses of asbestos samples collected from malignant mesothelioma cases in the province of Anatolia, the samples mostly contained chrysotile with associated tremolite (Turkish Mesothelioma Working Group, 2015; Metintaş *et al*., 2017). Until now, no detailed study using mineralogical analysis and geochemical modelling of the asbestos minerals of the Anatolian region has been carried out nor has the distribution of the chrysotile or tremolite minerals and their alteration been examined on a regional scale. Two possible hypothesized processes were tested to explain the serpentinization: 1) the effects of seawater on the accreted ophiolitic upper mantle crust and/or 2) long after the ophiolitic rock were uplifted and during/after the ophiolitic units were thrusted and interacted with hydrothermal/meteoric fluids along fractures. The main objective of the present study was to fill this knowledge gap and to identify the asbestos occurrences that cause health problems in central Anatolia.

GEOLOGICAL SETTING AND GENERAL FEATURES OF ASBESTOS MINERALS

Geological setting

The basement units of the study area consist of gneiss, quartz schist, amphibolite, and marble of the Paleozoic Kırşehir Massif (Kuşçu and Erler, 1998; Karadenizli, 2011). These units are cross-cut by Paleocene granites and granitoids and tectonically overlain by imbricated wedges of the Triassic Karakaya Complex, the Upper Cretaceous epi-ophiolitic sediments, and the Cretaceous Ankara Ophiolitic Mélange (AOM) of the İzmir-Ankara-Erzincan Suture Zone (IAESZ) (Figures 1, 2). The IAESZ formed when the Tethys ocean was closed during the NNE-directed convergence of Africa-Arabia with Eurasia during the latest Cretaceous – early Cenozoic (Sarıfakıoğlu *et al.*, 2017). Imbrication of ophiolitic units in IAESZ has a broad history that includes rift-drift, seafloor spreading, and subduction-zone development of the Neotethyan oceanic lithosphere from the early Triassic to the Late Cretaceous time interval (Sarıfakıoğlu *et al.*, 2017). The Cretaceous AOM is composed of Cretaceous ultramafic rocks, Cretaceous radiolarites, Cretaceous pillow basalts, and Upper Jurassic – Lower Cretaceous platform carbonate blocks set in a highly sheared and

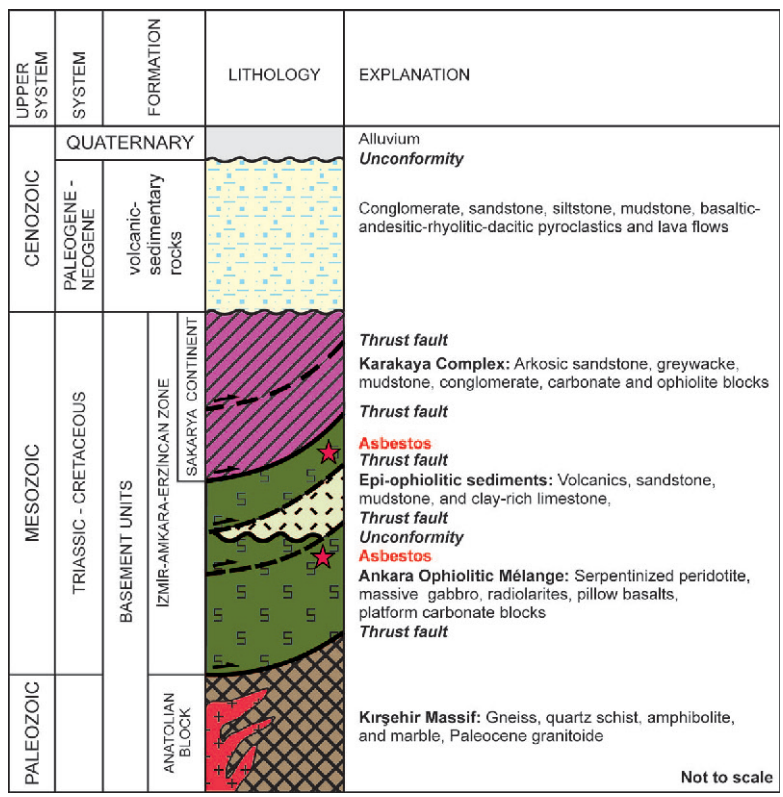

Figure 2. Stratigraphic section of the study area (modified from Sevin and Uğuz, 2011; Kadir *et al*., 2017). Stratigraphic symbols were defined in Figure 1.

https://doi.org/10.1346/CCMN.2018.064088 Published online by Cambridge University Press

brecciated ophiolitic detrital matrix (Rojay, 2013). The ophiolitic units of the AOM consist of serpentinized upper mantle peridotites that are mainly composed of harzburgite, dunite, localized pyroxenite, massive gabbro, plagiogranite intrusions, doleritic dikes, pillow basalt, and sheet flows (Dilek and Thy, 2006; Dangerfield *et al.*, 2011; Sarıfakıoğlu *et al.*, 2014, 2017). The Triassic Karakaya Complex overthrust the Cretaceous AOM (Rojay, 2013). Epi-ophiolitic sediments overlay the AOM along an angular unconformity and also tectonically overthrust the mélange because of multiple deformation phases (Dangerfield *et al.*, 2011). The absence of Eocene–Oligocene sedimentary units in the study area suggests that the region was subjected to uplift and chemical weathering (Şengör and Yılmaz, 1981; Yılmaz *et al*., 2000; Külah *et al*., 2014; Kadir *et al*., 2015). These units are overlain by Paleogene-Neogene volcanic and sedimentary units and by Quaternary alluvium (Figure 2).

General features of the asbestos minerals

The ophiolitic rocks of the IAESZ were thrust onto the Kırşehir Massif and imbricated along northward-dipping thrust faults during convergence of the Kırşehir block and the Sakarya-Pontide continent (Şengör and Yılmaz, 1981). These brecciated and intensely sheared units are hydrothermally altered (Dangerfield *et al.*, 2011, Çelik *et al*., 2013). Deformation of the dunite-harzburgite and pyroxenite rocks may be linked to serpentinization and chrysotile and/or tremolite formation along fault zones and fractures (Figures 3a–3h). The chrysotile either developed along the fracture surfaces or it covers the serpentinized dunite-harzburgite and pyroxenite units (Figures 3b–3h). Chrysotile+ tremolite crystals are up to 3 cm long (Figure 3). Locally, silica and chalcedony occur as fracture-infill developed as a result of hydrothermal alteration processes.

White-beige or pale green-beige soft fibrous chrysotile comprise compact bundles that are parallel to subparallel, 0.5–10 cm long, 1–3 mm thick, and are silky to touch (Figures 3i–3k), but localized occurrences of chrysotile are powdery to touch (Figures 3l, 3m). Chrysotile is widely exposed in the Karakoçaş, Şıhlar, Gürpınar, Gümerdiğin, Demirtaş, Kalecik, Kılıçlar, Deliler, Akçaviranşarşak, Yukarıyapançarşak, Karatekin, and Alpsarı areas (Figures 1; 3g–3m).

Tremolite, which formed as white–pale green aggregates on pyroxenite, are of relatively hard, compact fibers and fiber bundles in comparison to chrysotile. Tremolite crops out in the uninhabited Merzi pond and the Ahlat areas. These fibers are 1–5 cm long and generally are parallel to the fracture surfaces (Figures 1, 3n–3p).

White, pale green, thick, and fibrous chrysotile associated with tremolite crops out at the Değirmenkaya asbestos deposit and also occurs in the Gökdere, Çandır, Oyaca, and Beynam areas.

MATERIALS AND METHODS

Field work was carried out using the existing 1/500,000 scale geological maps of the Çankırı and Ankara regions (Figure 1; MTA, 2002) to identify the distribution of dunite-harzburgite and pyroxenite units and related asbestos materials in the study area. Up to 500 g of peridotite, bulk asbestos material, and claystone samples were collected from the various locations (Figure 1). Optical microscope studies using a Nikon-LV 100 Pol (Nikon Corporation, Tokyo, Japan) were carried out on fresh and partially altered dunite-harzburgite and pyroxenite rock samples. Selected samples that represent various degrees of alteration were manually crushed and powdered using a tungsten carbide pulverizer for X-ray diffraction (XRD) and geochemical analyses. The mineralogical characteristics of the samples were determined using powder X-ray diffractometry (XRD) with a Rigaku D/Max – 2200 with an Ultia PC (Rigaku Corporation, Tokyo, Japan). The XRD analyses were performed using CuKα radiation with a scanning speed of 1º2θ/min and a tube voltage and current of 40 kV and 30 mA, respectively. Bulk mineralogy was determined using random powder mounts. Semi-quantitative abundances of rock-forming minerals were determined using the sharp and unambiguous reflection intensities of the XRD patterns (Brindley, 1980a). The clay mineral relative abundances were determined using the basal reflections and the mineral intensity factors of Moore and Reynolds (1989). Representative chrysotile- and chrysotile-tremolite-dominated bulk samples were prepared for scanning electron microscopy-energy dispersive X-ray analysis (SEM-EDX) using double-sided tape to adhere the fresh, broken surface of each sample to an Al sample holder and by thinly coating the samples with fine Au particles (350 Å) using a Giko IB-3 ion coater (Giko Engineering Co. Ltd., Ama, Japan). The analyses were performed at Anadolu University (Turkey) using a Zeiss Supra™ 50 VP field emission (FE-SEM) instrument (Carl Zeiss AG, Jena, Germany). For transmission electron microscopic (TEM) analysis, chrysotile and tremolite particles were dispersed using an ultrasonic ethanol bath for 30 min, one drop of each clay suspension was placed on a C-coated Cu grid, and was dried at room temperature.

The chemical analyses of twenty asbestos, two claystone, and five peridotite host-rock samples were performed at the Bureau Veritas Mineral Laboratories (Vancouver, Canada) using a PerkinElmer Elan 9000 (PerkinElmer, Inc., Waltham, Massachusetts, USA) inductively coupled plasma–atomic emission spectrometer (ICP-AES), a mass spectrometer (ICP-MS), and a Spectro (Spectro Analytical Instruments Inc., Mahwah, New Jersey, USA) XLAB-2000 PED X-ray fluorescence spectrometer (PEDXRF), which was calibrated using USGS interlaboratory standards. The detection limits for the analyses were between 0.01 and 0.1 wt.% for major

https://doi.org/10.1346/CCMN.2018.064088 Published online by Cambridge University Press

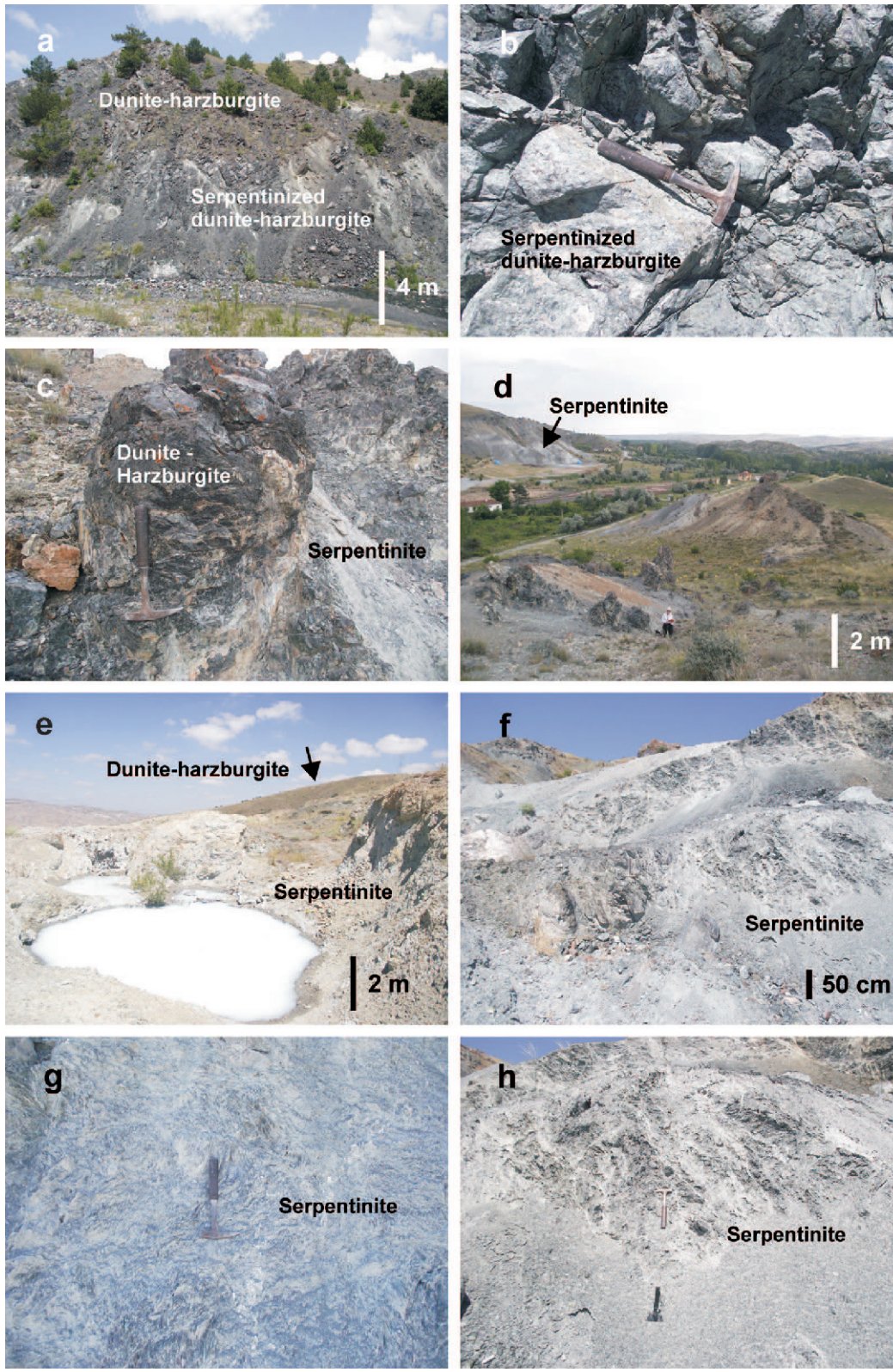

Figure 3. Field photographs of: (a) The serpentinized dunite-harzburgite in Merzi; (b) Close view of serpentinized dunite-harzburgite in Değirmenkaya; (c, d) Development of serpentinized material along tectonic zone in the Akçaviranşarşak and Alpsarı-Karatekin; (e–h) Views of serpentinized dunite-harzburgite in Değirmenkaya pit and Kalecik.

https://doi.org/10.1346/CCMN.2018.064088 Published online by Cambridge University Press

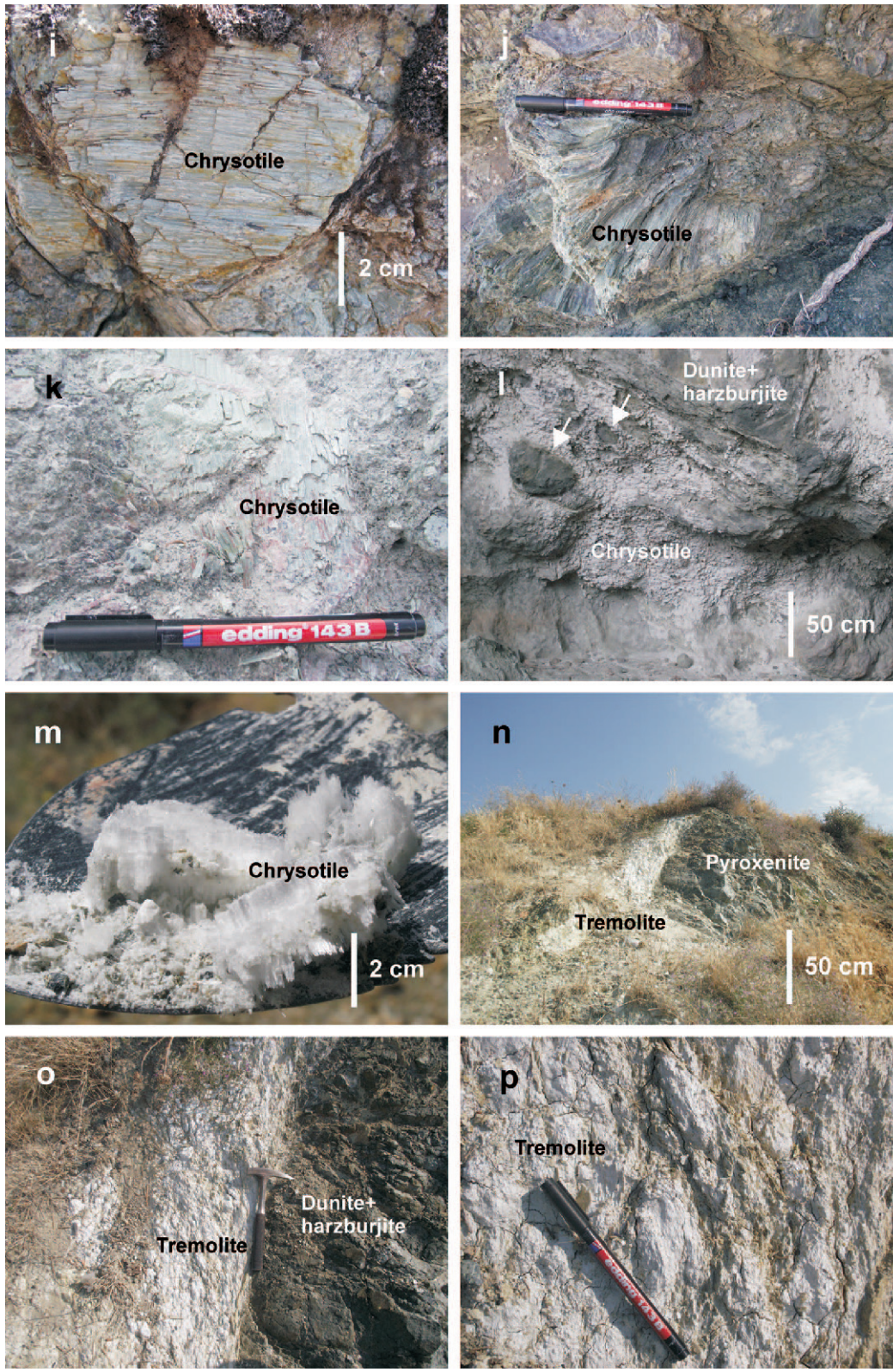

Figure 3 (*contd*.). Field photographs of: (i–m) Close view of chrysotile in Alpsarı, Gümerdiğin, Kalecik, Bakırlı, and Değirmenkaya; (n, o) Development of tremolite in pyroxenite units; and (p) Closeup view of tremolite.

https://doi.org/10.1346/CCMN.2018.064088 Published online by Cambridge University Press

elements, 0.1 and 5 ppm for trace elements, and 0.01 and 0.5 ppm for REE (Rare Earth Elements).

Fresh ultramafic units composed of dunite-harzburgite and pyroxenite that represent the host rock of the asbestos were used for mass gain and loss calculations. Mass gains and losses have been calculated and estimated using the EASYGRESGRANT program (López-Moro, 2012) and from isocon diagram plots of the geochemical analyses (Grant, 1986, 2005):

$$C_i^A = (M^O/M^A)C_i^O$$

where C_i is the concentration of component i, O indicates the fresh rock, and A indicates the altered rock. The M^O and M^A values are the equilibrium masses (as wt.% or ppm) of the fresh and altered rocks, respectively.

The C_i^A/C_i^O ratios were plotted to obtain the slopes of the isocon graphic lines from the fresh and the altered rock analytical data using the following equation:

$$\Delta C_i/C_i^O = (M^O/M^A)(C_i^A/C_i^O) - 1$$

where ΔC_i is the gain or loss of mass. The MnO, Na_2O, K_2O, and P_2O_5 were assumed to be immobile based on clusters of slopes that were close to 1.00.

If a constant mass is assumed,

$$\Delta C_i/C_i^O = (C_i^A/C_i^O) - 1$$

Thus, sample compositions that plot above the isocon line indicate a gain during the alteration process and samples that plot below this line represent a loss during alteration.

Chemical analyses were carried out on hand picked grains using a binocular microscope for one chrysotile and two tremolite samples. Analyses were obtained using a JEOL JSM2000FX2 (JEOL Ltd., Tokyo, Japan) analytical transmission electron microscope (ATEM) with a XMAXN 80 mm detector (Oxford Instruments, Abingdon, Oxfordshire, UK), and Oxford instruments INCA software for TEM at the Materials Department analytical facility of Imperial College, London, UK. The structural formulae of the chrysotile and tremolite were calculated based on $O_{10}(OH)_8$ and $O_{22}(OH)_2$ formulae, respectively (Page, 1968; Evans *et al*., 2000).

Fifteen tremolite and two chrysotile fractions were purified and analyzed for the H and O stable isotopes by the Cornell Isotope Laboratory at Cornell University, Ithaca, New York, USA. The isotope corrections were performed using a two-point normalization (regression) based on the international standards (IAEA CO-1 and IAEA CO-8) for $\delta^{18}O$ and CH-7 and benzoic acid for δ^2H. The analyses were performed using a Thermo Delta V (Thermo Fisher Scientific, Waltham, Massachusetts, USA) isotope ratio mass spectrometer interfaced to a temperature conversion elemental analyzer. The delta values for ^2H and ^{18}O were measured against a primary reference scale. The data are reported in the standard delta notation as per mil deviations from V-SMOW (Vienna Standard Mean Ocean Water).

The external reproducibility for $\delta^{18}O$ was ± 0.19‰ (1σ) and was based on repeated analyses of an internal white crystal standard. The NBS (National Bureau of Standards, U.S. National Institute for Standards and Technology, NIST) sample 28 (silica sand-optical) value is 9.61 ± 0.10‰ (1σ). The standard deviation for the internal standard benzoic acid was 1.01‰ for $\delta^{18}O$ and 1.24‰ for δ^2H.

RESULTS

Petrographic determinations

The host rocks of the chrysotile type serpentine consist of dunite and harzburgite (Figures 4a–4l). Olivine crystals are locally transformed to iddingsite (Figures 4a–4h). Serpentinization developed mostly along cleavage boundaries on or enclosing relict olivine, orthopyroxene (enstatite), and clinopyroxene (augite) crystals. The serpentinization results in non-pseudomorphic fiber bundles and mesh texture asbestos minerals similar to that reported by Wicks and Whittaker (1977) (Figures 4a–4g, 4i–4k). The degree of serpentinization increases from the marginal mesh rim of olivine and enstatite outwards (Figures 4a–4h). Serpentinization is also associated with silica phases that fill micro-veins in fractured olivine (Figures 4a–4c). Chrysotile forms a mesh of fiber bundles (0.21–0.63 mm long and 0.1 to 0.21 mm in diameter) that are suboriented to oriented longways and fibers that fill millimeter micro-vein textures (Figures 4g–4h). These highly serpentinized olivine and enstatite components also enclose opaque minerals, such as vermiform magnetite phases (Figure 4h). Subhedral enstatite crystals associated with serpentinized olivine are mostly converted to oxyenstatite (Figures 4d–4f).

The host rock of the tremolite is a pyroxenite that is composed of abundant augite associated with minor olivine. The augite and olivine are mostly degraded and are either locally or completely converted to tremolite fiber bundles (Figures 4i–4k). The fiber bundles are bent, which is possibly the result of tectonism (Figure 4k). Locally, pyroxene crystals are chloritized (Figure 4l).

XRD determination

The results of XRD analyses of the bulk asbestos samples are presented in Table 1. Chrysotile is abundant relative to tremolite in the study area. Both chrysotile and tremolite are associated with chlorite. Chrysotile was distinguished by very sharp diagnostic reflections at 7.27–7.35 Å and 3.63–3.66 Å and tremolite was distinguished by sharp reflections at 8.40, 8.42, and 3.12–3.13 Å. Hydromagnesite was identified by reflections at 9.28–9.26, 5.81, and 2.90 Å, olivine by reflections at 2.85, 2.51, 2.50, and 2.30 Å, and pyroxene by reflections at 3.17, 3.03, 2.89–2.94, 2.56, and 2.52 Å (Figure 5). Claystone samples that are composed of smectite, chlorite, kaolinite, and illite are associated with pyroxene, olivine, and quartz (Figure 5).

https://doi.org/10.1346/CCMN.2018.064088 Published online by Cambridge University Press

Table 1. Mineralogical compositions of the samples in the Çankırı and Ankara regions. Note the abbreviations: Ctl = chrysotile; Tr = tremolite; Chl = chlorite; Sme = smectite; Ilt = illite; Kln = kaolinite; Gth = goethite; Qz = quartz; Opl = opal-CT; Hmgs = hydromagnesite; Ol = olivine; Px = pyroxene; acc = accessory; and + = the relative abundance of the minerals. (abbreviations after Whitney and Evans, 2010).

	Ctl	Tr	Chl	Sme	Ilt	Kln	Gth	Qz	Opl	Hmgs	Ol	Px
Karatepe-Şıhlar												
SIH-14	+++++		acc									
Ahlat												
AHL-1	+++++											
AHL-3		+++	++									
Merzi Göleti												
MRZ2-1	+	++++										
MRZ2-3			+++			+					+	+
Alpsarı												
ASR3-1	+++++											acc
ASR3-2	+++++		acc									
Karatekin												
KTK1-1	+++++											
Gürpınar												
GPR-1	++++											+
Çapar												
CPR-3	++	++	+									acc
Bakırlı												
BKR-4	++	+						acc			++	
BKR-5	++	+									+	acc
Gümerdiğin												
GMR-1	++							+			acc	++
GMR-4	+++++											
Karakoçaş												
KKC3-2							acc		acc	++++	acc	+
KKC3-3	+++											++
KKC3-7	+++++											
Demirtaş												
DMT-6	+++++											
Değirmenkaya												
DGK-1	++								++		acc	+
DGK-2	++							+				++
Kalecik												
KLC-2	++++									acc		
Gökdere												
GDR-1	++++		acc									+
GDR-3	++++	acc		+							acc	+
Kılıçlar												
KLR-1	+++++											acc
KLR-8	+++++											
KLR-9			+	++	+	+		acc				+
Deliler												
DLL-1	+++++		acc									acc
Beynam Orman İçi												
BOI-1	++	++		+				acc			acc	+
Oyaca												
OYC-1	++	++	+								acc	acc
Yukarıyapançarşak												
YYC-1	++++											+
YYC-4	+++++	acc										
Akçavirançarşak												
AVC-1	++++	acc	+									

https://doi.org/10.1346/CCMN.2018.064088 Published online by Cambridge University Press

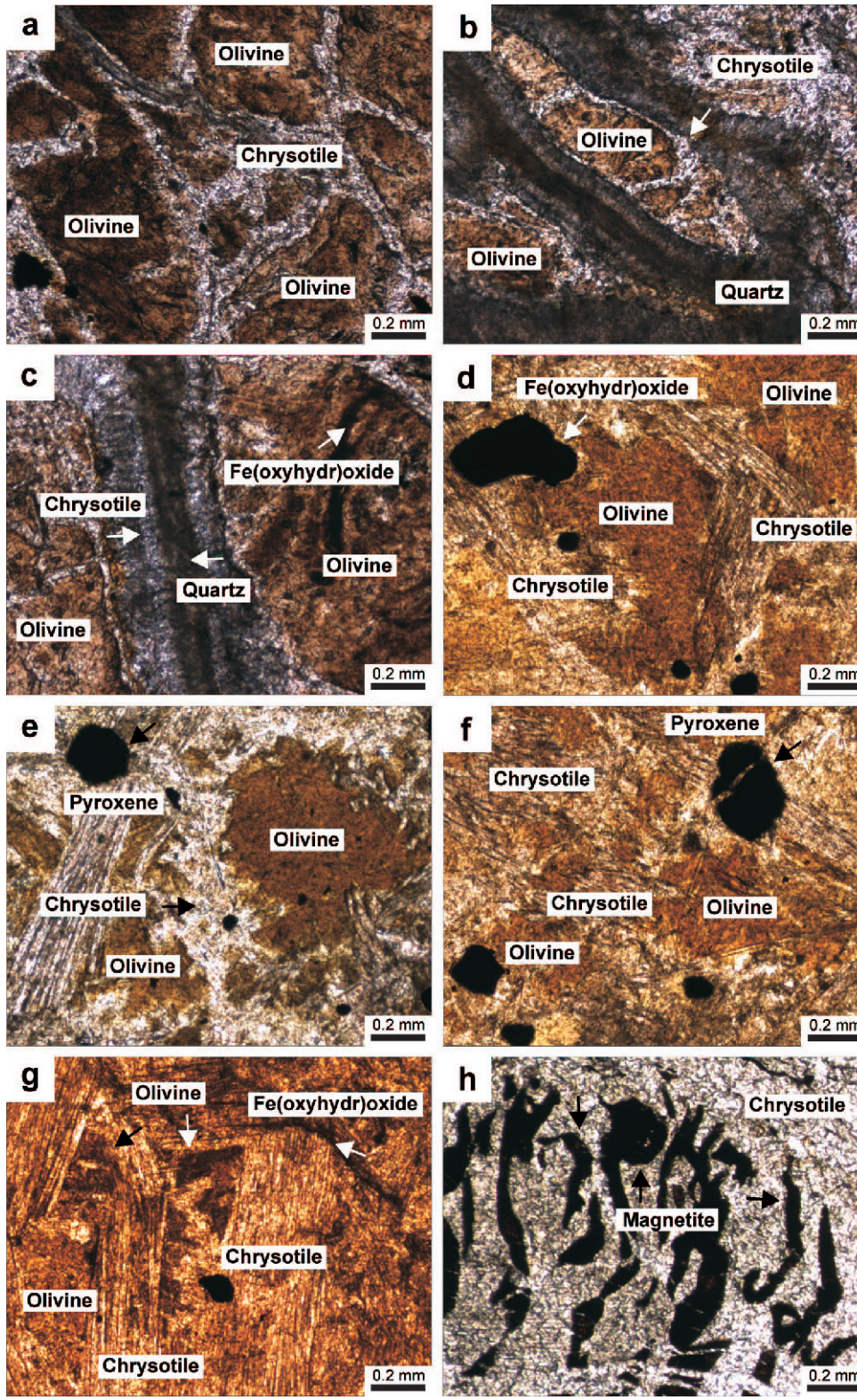

Figure 4. Photomicrographs of (a, b) Development of chrysotile along cleavage boundaries on relict olivine crystals viewed under plane-polarized light (BKR-1); (c) Closeup view of (a, b) viewed under plane-polarized light (BKR-1); (d–g) Sub-oriented to oriented long fiber bundle of chrysotile developed on relict olivine and enstatite crystals viewed under plane-polarized light (AVC-2); (h) Vermiform magnetite in serpentinized olivine under plane-polarized light (EDV-1).

https://doi.org/10.1346/CCMN.2018.064088 Published online by Cambridge University Press

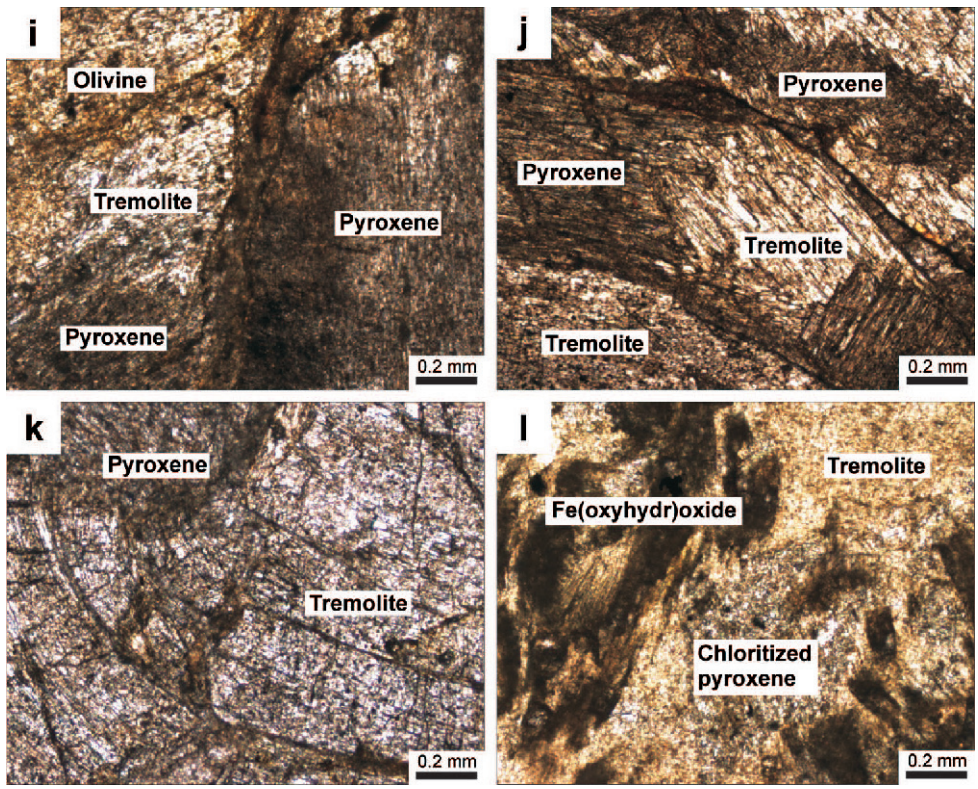

Figure 4 (*contd*.). (i) Development of tremolite between relict augite and olivine crystals viewed under plane-polarized light (BOI-1); (j, k) Close relationship between tremolite and relict augite viewed under plane-polarized light (BOI-1); and (l) Tremolite associated with Fe(oxhydr)oxide and enclosing chloritized pyroxene viewed under plane-polarized light (AVC-2).

Smectite was identified by a poorly crystalline reflection between 7 and 9º2θ, that expands to 17.06 Å after solvation with ethylene glycol and collapses to 9.69 Å after heating at 550ºC for 2 h (Figure 5). The 9.98, 4.95, and 1.52 Å peaks are consistent with a trioctahedral illite (Moore and Reynolds, 1989). Chlorite was identified from the sharp reflections at 14.17 and 4.71 Å that did not shift after ethylene-glycol treatment or after heating at 350ºC and 550ºC. Kaolinite was identified from reflections at 7.09 and 3.57 Å that were not affected by ethylene-glycol treatment or heating at 350ºC, but collapsed upon heating at 550ºC (Figure 5).

SEM-EDX determinations

Chrysotile and local tremolite are abundant in the serpentinized dunite-harzburgite and pyroxenite (Figure 6). Chrysotile fibers are 1–10 μm long and 80–150 nm thick that developed either as bundles, knitted aggregates, or as a mesh on ferromagnesian precursors, such as olivine, pyroxene, and serpentinized olivine (Figures 6a–6g). Tremolite fibers are 15–300 μm long and 50–100 nm thick and developed as fiber bundles and knitted aggregates (Figures 6h–6l). These fibers and fiber bundles either enclose or coat relict pyroxene crystals (Figures 6j, 6k). Tremolite fiber bundles also enclose 2.30 μm diameter spherical structures that resemble opal-CT (Figure 6h). Locally, hydromagnesite crystals have a platy character and occur in association with tremolite fiber bundles (Kadir *et al*., 2012; Figures 6m, 6n).

Geochemistry

Whole-rock chemical analyses of fresh and altered samples from the study area are given in Table 2. The peridotite samples contain Al_2O_3 (avg. 0.90–2.74 wt.%), ΣFe_2O_3 (avg. 7.14–10.59 wt.%), SiO_2 (avg. 37.37–43.12 wt.%), MgO (avg. 29.36–38.05 wt.%), CaO (0.04–3.20 wt.%), and Cr_2O_3 (0.331–0.784 wt.%) with loss on ignition (LOI) values that averaged 9.6–14.3-wt.%. The asbestos samples were characterized by Al_2O_3 (0.1–2.65 wt.%), ΣFe_2O_3 (1.69–11.95 wt.%), SiO_2 (35.32–45.76 wt.%), MgO (31.87–37.06 wt.%), CaO (0.03–3.21 wt.%), and Cr_2O_3 (<0.002–0.948 wt.%) contents with LOI values of 11.8–22.30 wt.%. Claystone samples contain Al_2O_3 (5.41–14.52 wt.%), ΣFe_2O_3 (3.34–6.72 wt.%), SiO_2 (44.41–49.36 wt.%), MgO (16.39–19,38 wt.%), CaO (8.01–8.71 wt.%), and Cr_2O_3 (0.025–0.090 wt.%) with LOI values of 7.1–12.4 wt.%.

The respective ranges in Ni and Co values were 1689–2314 ppm and 94.2–111.1 ppm in peridotite, 377–2314 ppm and 16.6–105.5 ppm in asbestos, and 166–452 and 23–60.1 ppm in claystone samples. Rare

https://doi.org/10.1346/CCMN.2018.064088 Published online by Cambridge University Press

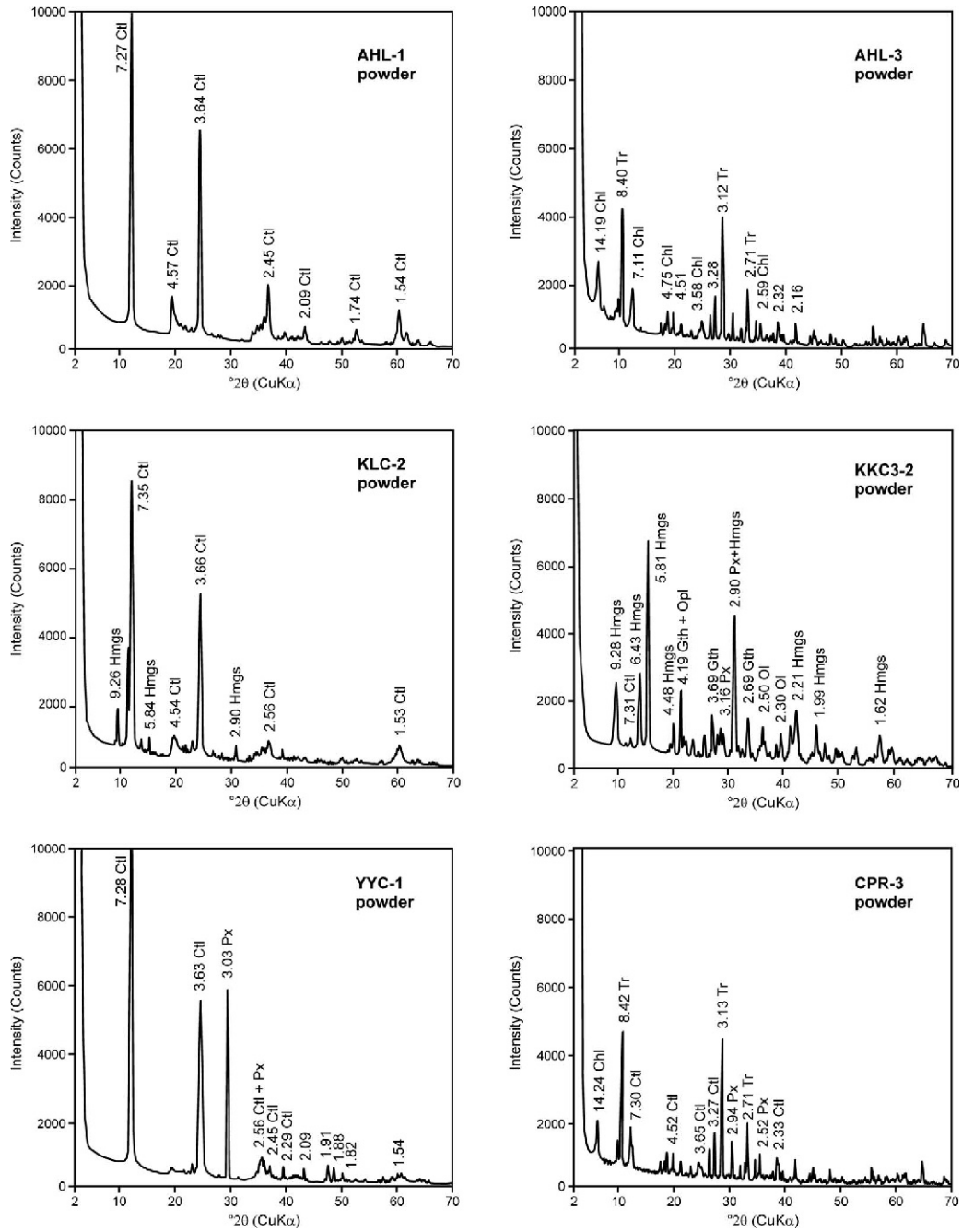

Figure 5. X-ray diffraction patterns of the chrysotile- and chrysotile+tremolite-rich asbestos and claystone samples in the Çankırı and Ankara regions. Note the abbreviations: Ctl = chrysotile; Tr = tremolite; Chl = chlorite; Sme = smectite; Ilt = illite; Kln = kaolinite; Gth = goethite; Qz = quartz; Opl = opal-CT; Hmgs = hydromagnesite; Ol = olivine; Px = pyroxene (abbreviations after Whitney and Evans, 2010).

earth element (*REE*) data for the handpicked asbestos samples were normalized to the composition of chondrite meteorites and the primitive mantle (Sun and McDonough, 1989; Table 2; Figures 7a, 7b). The asbestos samples have flat *REE* patterns. Light rare earth elements (*LREE*) show an enrichment relative to the middle rare earth elements (*MREE*) and heavy rare earth elements (*HREE*) with negative to positive Eu (0.36–1.88) values and positive Ce (1.88–4.86) anomalies (Figure 7a). The Rb, Ba, Ce, Pr, Sr, Zr, and Y contents were depleted relative to the primitive mantle (Figure 7b).

The mass gains and losses were based on calculated delta (ΔC_I) values and isocon diagram plots of the

https://doi.org/10.1346/CCMN.2018.064088 Published online by Cambridge University Press

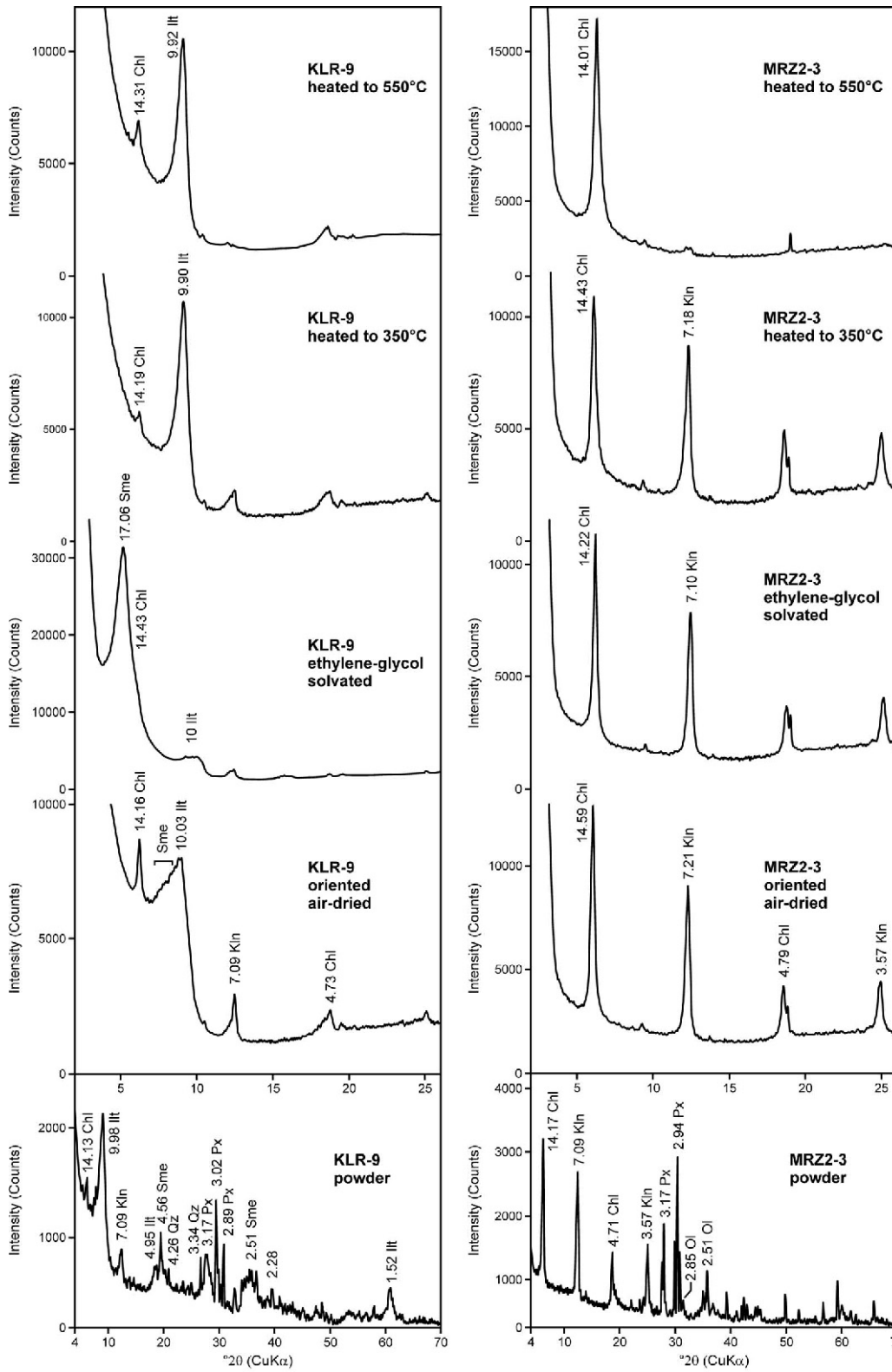

Figure 5 (*contd*.). X-ray diffraction patterns of the chrysotile- and chrysotile+tremolite-rich asbestos and claystone samples in the Çankırı and Ankara regions. Note the abbreviations: Ctl = chrysotile; Chl = chlorite; Sme = smectite; Ilt = illite; Kln = kaolinite; Ol = olivine; Px = pyroxene (abbreviations after Whitney and Evans, 2010).

https://doi.org/10.1346/CCMN.2018.064088 Published online by Cambridge University Press

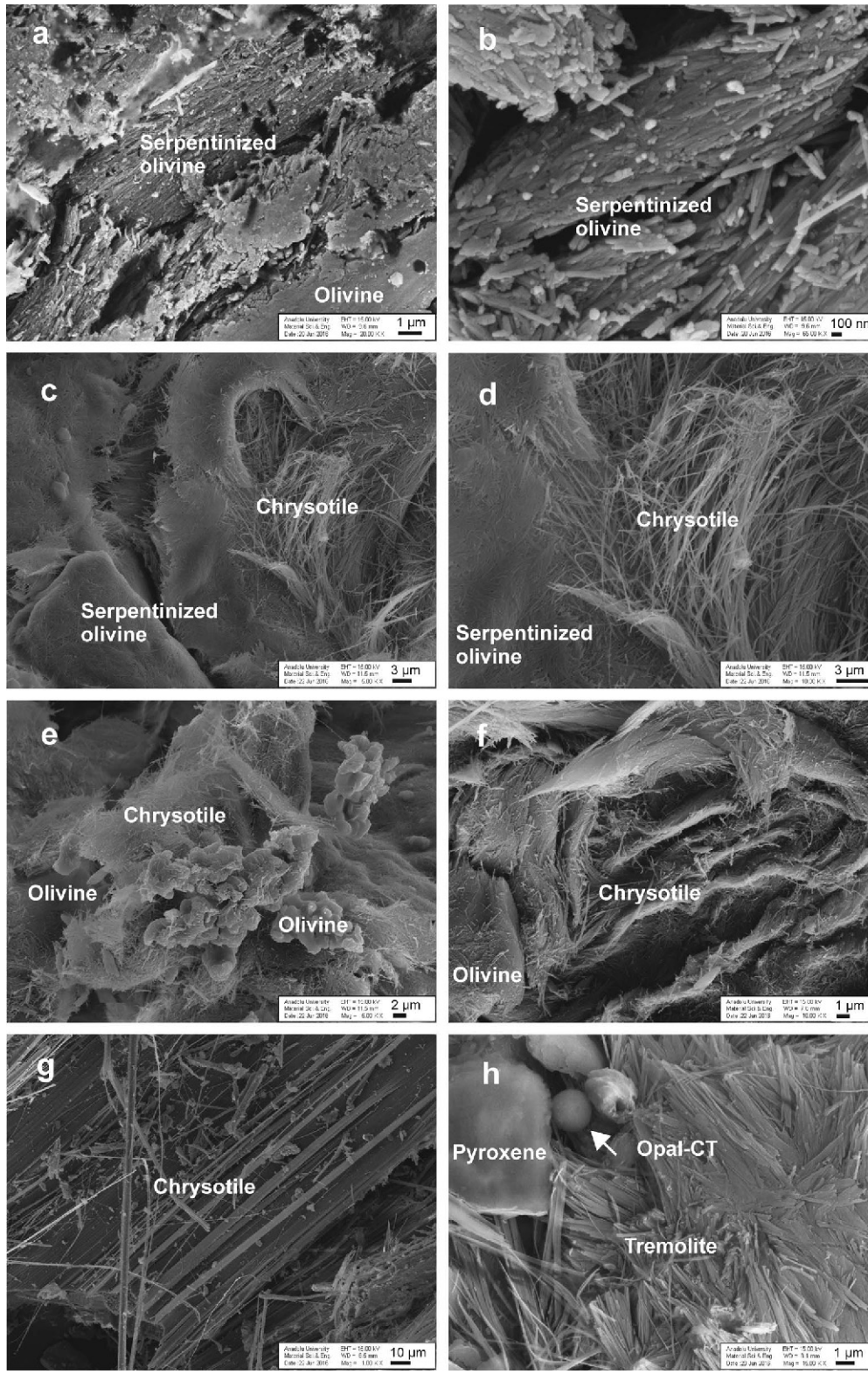

Figure 6. SEM images: (a, b) Serpentinized olivine (AHL-1); (c) Serpentinized olivine edging fibrous chrysotile (DGK-1); (d) Close view of (c); (e, f) Parallel to subparallel fiber bundles and mesh of chrysotile enclosing relict of olivine (DGK-1, BKR-4); (g) Subparallel fiber bundles of chrysotile (GPR-1); (h) Subparallel fiber bundles of tremolite associated with relict of pyroxene and spherical opal-CT (MRZ2-1).

https://doi.org/10.1346/CCMN.2018.064088 Published online by Cambridge University Press

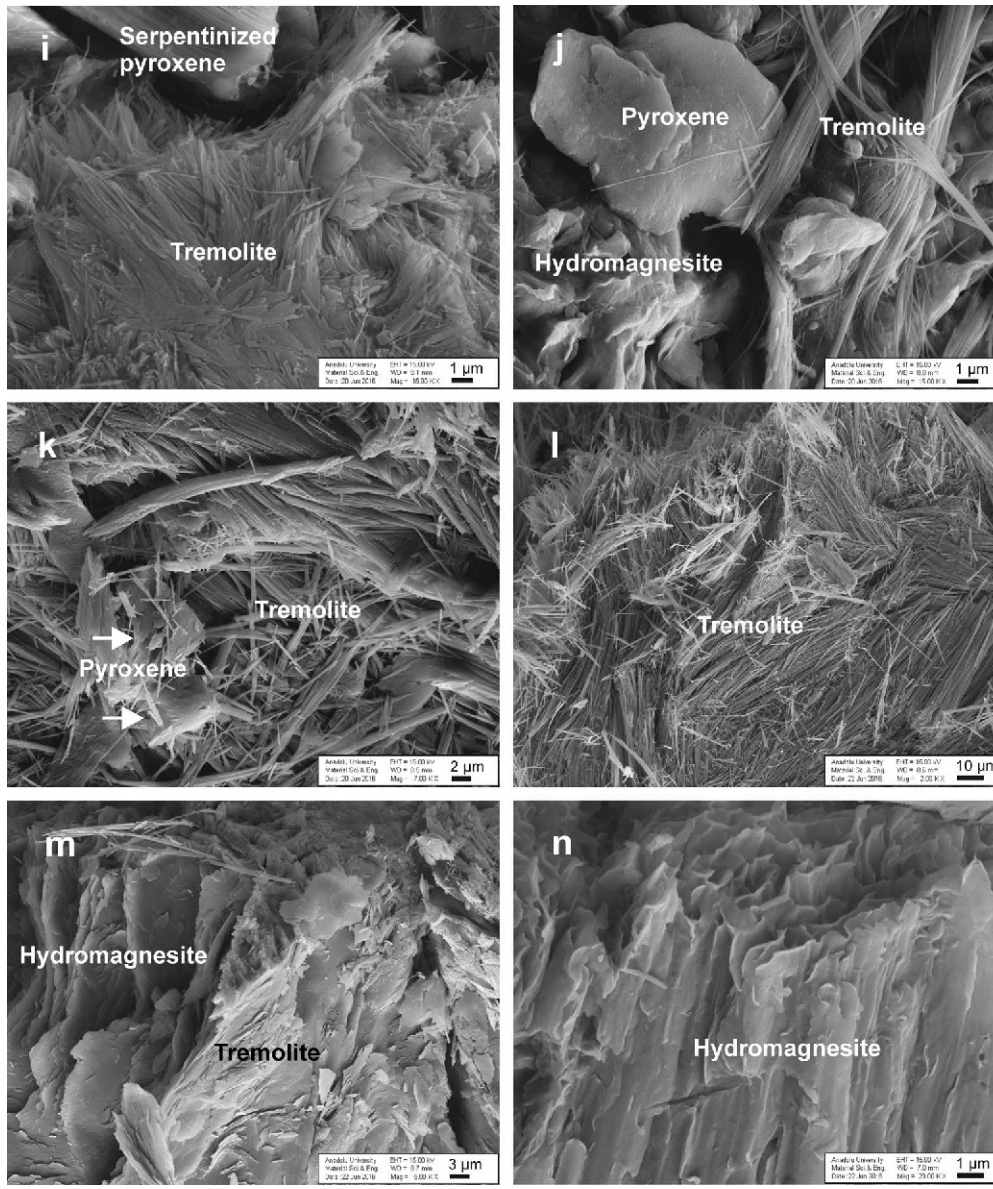

Figure 6 (*contd.*). (i) Subparallel fiber bundles of tremolite associated with relict of pyroxene (MRZ2-1); (j) Fibrous tremolite enclosing pyroxene and hydromagnesite crystals (MRZ2-1); (k, l) Sub-parallel fiber bundles and meshes of tremolite that enclose relict of pyroxene (AHL-3, GPR-3); (m) Platy hydromagnesite association with tremolite (GPR-3); and (n) Sub-parallel orientation of hydromagnesite plates (KKC3-2).

geochemical analyses (Grant, 1986, 2005) show that MgO, Fe_2O_3, Al_2O_3, Ni, Cr, and Nb were depleted, while SiO_2, TiO_2, CaO, Zr, Y, Th, La, Sr, Pr, Nd, and Sm were enriched during serpentinization based on the isocon slope (m = 1) (Table 3; Figure 8). The MnO and Pb ΔC_i values indicate an immobile character.

Mineral chemistry

The structural formulae of chrysotile and tremolite were calculated on the basis of ATEM chemical analyses (Table 4). The tetrahedral sites (T) are occupied by Si, which is partially substituted by Al in chrysotile and Al+Fe in tremolite. Mg is prevalent in the octahedral sites (C) and is associated with Al+Fe+Ca+Mn in chrysotile and Fe in tremolite. In addition, excess Ca, Mg, and Mn in tremolite occupy site B and Na+K in chrysotile and tremolite is thought to occupy site A. The A, B, and C structural cation sites in chrysotile and tremolite were based on the work of Liu *et al.* (2011), Della Ventura *et al.* (2014), and Kadir and Erkoyun (2015).

Stable isotopes

The oxygen- and hydrogen-isotopic compositions of the chrysotile and chrysotile+tremolite samples are

https://doi.org/10.1346/CCMN.2018.064088 Published online by Cambridge University Press

Table 2. Major (wt.%) and trace element (ppm) compositions of the peridotite, asbestos, and claystone samples in the study area. Note: Σ*REE* = the sum of (La–Lu)+Y; Σ*LREE* = the sum of La–Nd; Σ*MREE* = the sum of (Sm–Ho); Σ*HREE* = the sum of (Er–Lu); Eu/Eu* = $Eu_N/[(Sm_N \times 0.67)+(Tb_N \times 0.33)]$ (Bau and Dulski, 1996); Ce/Ce* = $0.5La_N+0.5Pr_N$ (Dai *et al*., 2016); and LOI = loss on ignition at 1050ºC.

Major oxides	Peridotite						Asbestos			
(wt.%)	EDV-1	AVC-2	DLL-2	SIH-13	GMR-6	Avg.	GDR-5	AVC-1a	SIH-17	DGK-3
SiO_2	39.76	43.12	38.86	37.37	40.54	39.93	40.8	40.34	35.32	35.73
Al_2O_3	0.90	2.74	1.21	0.91	0.89	1.33	1.26	2.65	1.04	0.98
ΣFe_2O_3	7.25	10.59	7.26	8.74	7.14	8.20	6.74	11.95	8.27	6.16
MgO	38.05	29.36	37.98	37.72	36.54	35.93	34.33	31.87	34.62	37.41
CaO	0.15	3.20	0.04	0.14	0.30	0.80	2.50	0.83	3.64	0.64
Na_2O	<0.01	0.01	<0.01	<0.01	<0.01	<0.01	0.02	<0.01	<0.01	<0.01
K_2O	<0.01	<0.01	<0.01	<0.01	<0.01	<0.01	0.04	<0.01	<0.01	<0.01
TiO_2	<0.01	0.05	0.02	<0.01	<0.01	<0.02	0.04	0.05	0.02	0.02
P_2O_5	<0.01	<0.01	<0.01	<0.01	<0.01	<0.01	<0.01	<0.01	<0.01	<0.01
MnO	0.08	0.16	0.09	0.11	0.11	0.11	0.12	0.24	0.09	0.12
Cr_2O_3	0.370	0.784	0.442	0.331	0.359	0.457	0.289	0.948	0.266	0.392
LOI	13.0	9.6	13.7	14.3	13.2	12.8	13.8	10.9	15.9	17.6
Total	99.82	99.83	99.87	99.88	99.37	99.75	99.83	99.87	99.40	99.33
Trace elements (ppm)										
Ni	2109	1689	2079	2314	2057	2050	1727	1112	1597	1807
Cr	2531	5364	3024	2265	2456	2607	1977	6486	1820	2682
Sc	9	18	11	8	10	11.2	8	20	8	8
Ba	<1	3	<1	<1	5	<2.2	10	2	6	20
Be	<1	<1	<1	<1	<1	<1	2	<1	<1	<1
Co	96.7	111.1	94.2	106.1	109.7	103.7	90.7	98.6	87.6	82.8
Cs	<0.1	<0.1	<0.1	<0.1	<0.1	<0.1	<0.1	<0.1	<0.1	<0.1
Ga	0.8	3.2	<0.5	0.6	3.8	<1.8	1.4	3.5	3.9	3.4
Hf	<0.1	0.1	<0.1	<0.1	<0.1	<0.1	0.1	<0.1	<0.1	<0.1
Nb	0.3	4.6	0.1	0.2	<0.1	<1.1	0.7	0.4	<0.1	<0.1
Rb	<0.1	0.3	0.1	0.1	0.3	<0.2	1.4	0.2	0.3	0.4
Sn	<1	<1	<1	<1	<1	<1	<1	<1	<1	<1
Sr	3.4	16.2	0.9	1.6	22.9	9.0	42.2	13.3	35.4	38.0
Ta	<0.1	<0.1	<0.1	<0.1	0.1	<0.1	<0.1	<0.1	0.1	<0.1
Th	<0.2	<0.2	<0.2	<0.2	<0.2	<0.2	<0.2	<0.2	<0.2	<0.2
U	<0.1	<0.1	<0.1	<0.1	<0.1	<0.1	0.2	0.1	1.0	<0.1
V	55	141	51	39	53	68	52	194	47	37
W	<0.5	<0.5	<0.5	<0.5	1.4	<0.7	<0.5	<0.5	1.6	1.9
Zr	0.2	11.8	0.5	0.1	0.4	2.6	4.3	1.1	0.7	1.0
Y	0.2	1.1	0.2	<0.1	0.2	<0.4	1.0	0.9	0.6	0.6
La	0.2	0.2	0.1	<0.1	<0.1	<0.1	0.9	0.4	<0.1	0.2
Ce	0.2	0.3	0.2	<0.1	<0.1	<0.2	1.3	0.6	0.2	<0.1
Pr	0.03	0.03	0.05	<0.02	<0.02	<0.03	0.17	0.09	<0.02	<0.02
Nd	<0.3	<0.3	<0.3	<0.3	<0.3	<0.3	0.8	<0.3	<0.3	<0.3
Sm	<0.05	<0.05	<0.05	<0.05	<0.05	<0.05	0.14	<0.05	<0.05	<0.05
Eu	<0.02	0.03	<0.02	<0.02	<0.02	<0.02	0.06	<0.02	<0.02	<0.02
Gd	<0.05	0.09	<0.05	<0.05	<0.05	<0.06	0.16	0.11	<0.05	0.05
Tb	<0.01	0.02	<0.01	<0.01	<0.01	<0.01	0.03	0.02	<0.01	0.02
Dy	<0.05	0.15	0.07	<0.05	<0.05	<0.07	0.17	0.15	0.07	0.15
Ho	<0.02	0.04	<0.02	<0.02	<0.02	<0.02	0.04	0.04	<0.02	<0.02
Er	<0.03	0.14	0.04	<0.03	0.05	<0.06	0.13	0.11	0.09	0.10
Tm	<0.01	0.02	<0.01	<0.01	<0.01	<0.01	0.02	0.02	<0.01	<0.01
Yb	<0.05	0.13	<0.05	<0.05	0.06	<0.07	0.14	0.15	<0.05	0.07
Lu	0.01	0.03	<0.01	<0.01	<0.01	<0.01	0.02	0.03	0.02	<0.01
TOT/C	0.05	<0.02	0.03	0.18	0.11	<0.08	0.62	0.03	1.45	2.02
TOT/S	<0.02	<0.02	<0.02	<0.02	0.04	<0.03	<0.02	<0.02	<0.02	<0.02
Mo	1.2	<0.1	<0.1	<0.1	0.2	<0.3	0.1	<0.1	0.2	0.2
Cu	6.9	3.0	7.7	4.2	10.4	6.4	44.2	2.2	14.1	15.6
Pb	0.2	0.1	<0.1	<0.1	0.4	<0.2	0.7	0.3	0.2	0.2
Zn	23	21	27	19	19	22	58	34	21	20
As	4.9	<0.5	<0.5	<0.5	0.5	<1.4	1.3	<0.5	1.6	2.8
Cd	<0.1	<0.1	<0.1	<0.1	<0.1	<0.1	<0.1	<0.1	<0.1	<0.1
Sb	<0.1	<0.1	<0.1	<0.1	<0.1	<0.1	<0.1	<0.1	<0.1	<0.1
Bi	<0.1	<0.1	<0.1	<0.1	<0.1	<0.1	<0.1	<0.1	<0.1	<0.1
Ag	<0.1	<0.1	<0.1	<0.1	<0.1	<0.1	<0.1	<0.1	<0.1	<0.1
Au (ppb)	1.0	0.9	1.6	<0.5	2.1	<1.2	1.3	<0.5	2.2	2.6
Hg	<0.01	<0.01	<0.01	0.01	0.02	<0.01	<0.01	<0.01	<0.01	<0.01
Tl	<0.1	<0.1	<0.1	<0.1	<0.1	<0.1	<0.1	<0.1	<0.1	<0.1
Se	<0.5	<0.5	<0.5	<0.5	<0.5	<0.5	<0.5	<0.5	<0.5	<0.5
Σ*REE*	1.23	2.63	1.18	0.92	1.05	1.40	5.08	2.99	1.61	1.72
Σ*LREE*	0.73	0.83	0.65	0.52	0.52	0,65	3.17	1.39	0.62	0.62
Σ*MREE*	0.20	0.38	0.22	0.20	0.20	1.2	0.60	0.39	0.22	0.31
Σ*HREE*	0.10	0.32	0.11	0.10	0.13	0.15	0.31	0.31	0.17	0.19
Eu/Eu*	0.30	0.39	0.30	0.30	0.30	0.32	0.64	0.39	0.30	0.39
Ce/Ce*	0.58	0.58	0.47	0.31	0.31	0.45	3.69	1.31	0.31	0.52

https://doi.org/10.1346/CCMN.2018.064088 Published online by Cambridge University Press

Table 2 (*contd*.)

Major oxides (wt.%)	Asbestos									
	KLC-2	YYC-4	AVC-1	GDR-1	KLR-8	DLL-1	SIH-14	AHL-1	ASR3-1	KTK1-1
SiO_2	37.9	45.13	42.48	43.68	46.61	44.39	42.11	45.76	41.78	40.38
Al_2O_3	0.18	0.16	2.39	0.51	0.56	0.46	0.97	1.04	1.69	1.82
ΣFe_2O_3	8.41	6.83	11.12	3.85	3.31	3.03	6.7	1.69	3.33	4.84
MgO	35.52	35.12	29.66	34.06	36.16	36.38	35.02	37.06	34.95	32.93
CaO	0.17	0.11	0.67	2.22	0.04	1.32	0.24	0.03	3.04	3.21
Na_2O	<0.01	<0.01	<0.01	<0.01	<0.01	<0.01	<0.01	<0.01	<0.01	<0.01
K_2O	<0.01	<0.01	<0.01	<0.01	<0.01	<0.01	<0.01	<0.01	<0.01	0.01
TiO_2	<0.01	<0.01	0.04	<0.01	<0.01	0.02	0.01	<0.01	0.03	0.04
P_2O_5	<0.01	<0.01	<0.01	<0.01	<0.01	<0.01	<0.01	<0.01	<0.01	<0.01
MnO	0.05	0.08	0.24	0.15	0.06	0.08	0.1	0.05	0.14	0.08
Cr_2O_3	0.161	0.002	0.896	<0.002	0.024	0.009	0.306	0.01	0.004	0.069
LOI	16.9	12	11.8	14.8	12.5	13.6	13.6	13.7	14.4	16
Total	99.41	99.42	99.46	99.43	99.41	99.4	99.38	99.4	99.42	99.45
Trace elements (ppm)										
Ni	1183	377	965	1046	1225	626	2240	672	405	780
Cr	1102	14	6130	<14	164	62	2094	68	27	472
Sc	5	<1	16	<1	2	2	6	2	2	4
Ba	<1	<1	2	5	<1	<1	3	2	<1	7
Be	2	<1	<1	<1	<1	<1	<1	<1	<1	<1
Co	68.3	98.2	105	56.2	65.5	42.8	105.5	16.6	77.3	54.1
Cs	<0.1	<0.1	<0.1	<0.1	<0.1	<0.1	<0.1	<0.1	<0.1	<0.1
Ga	<0.5	<0.5	3.2	<0.5	<0.5	<0.5	<0.5	<0.5	1	1.4
Hf	<0.1	<0.1	<0.1	<0.1	<0.1	<0.1	<0.1	<0.1	<0.1	<0.1
Nb	<0.1	<0.1	<0.1	<0.1	<0.1	0.3	1	0.1	<0.1	0.2
Rb	<0.1	<0.1	0.3	<0.1	<0.1	<0.1	0.3	<0.1	<0.1	0.5
Sn	<1	<1	<1	<1	<1	<1	7	<1	<1	<1
Sr	<0.5	2.6	19	100.2	0.8	55.8	1.3	1	16.5	20.6
Ta	0.1	<0.1	<0.1	<0.1	<0.1	<0.1	<0.1	<0.1	<0.1	<0.1
Th	<0.2	<0.2	<0.2	<0.2	<0.2	<0.2	<0.2	<0.2	<0.2	<0.2
U	<0.1	<0.1	0.1	0.5	<0.1	<0.1	<0.1	2.4	<0.1	<0.1
V	<8	<8	161	<8	10	11	25	38	42	36
W	<0.5	<0.5	<0.5	<0.5	<0.5	0.8	<0.5	<0.5	<0.5	<0.5
Zr	0.3	0.1	1.5	0.7	0.2	0.6	2.1	0.7	0.5	1.7
Y	<0.1	<0.1	0.9	<0.1	<0.1	<0.1	0.4	0.2	0.6	1.2
La	0.3	0.2	0.2	0.3	0.1	0.4	0.4	0.3	0.2	0.4
Ce	0.1	<0.1	0.3	0.2	<0.1	0.2	0.5	0.3	0.1	0.6
Pr	<0.02	<0.02	<0.02	<0.02	<0.02	<0.02	0.04	<0.02	<0.02	0.07
Nd	<0.3	<0.3	<0.3	<0.3	<0.3	<0.3	<0.3	<0.3	<0.3	<0.3
Sm	<0.05	<0.05	<0.05	<0.05	<0.05	<0.05	<0.05	<0.05	<0.05	<0.05
Eu	<0.02	<0.02	<0.02	<0.02	<0.02	<0.02	<0.02	<0.02	0.02	0.03
Gd	<0.05	<0.05	0.07	<0.05	<0.05	<0.05	0.06	<0.05	0.07	0.11
Tb	<0.01	<0.01	0.01	<0.01	<0.01	<0.01	0.02	<0.01	<0.01	0.02
Dy	<0.05	<0.05	0.14	<0.05	<0.05	<0.05	0.06	<0.05	0.07	0.21
Ho	<0.02	<0.02	<0.02	<0.02	<0.02	<0.02	<0.02	<0.02	<0.02	0.04
Er	0.03	<0.03	0.13	<0.03	<0.03	<0.03	0.06	<0.03	0.08	0.13
Tm	<0.01	<0.01	0.02	<0.01	<0.01	<0.01	0.02	<0.01	<0.01	0.02
Yb	<0.05	<0.05	0.14	<0.05	<0.05	<0.05	0.1	<0.05	0.08	0.16
Lu	<0.01	<0.01	0.02	<0.01	<0.01	<0.01	0.01	<0.01	<0.01	0.02
TOT/C	0.89	0.06	0.07	1.01	0.02	0.65	0.04	0.02	0.88	1.35
TOT/S	0.02	<0.02	<0.02	<0.02	<0.02	0.07	<0.02	<0.02	<0.02	<0.02
Mo	0.2	<0.1	<0.1	<0.1	<0.1	<0.1	<0.1	<0.1	<0.1	<0.1
Cu	0.9	0.8	2.8	0.8	2.2	0.3	7.7	9.2	2.9	19.2
Pb	<0.1	<0.1	<0.1	<0.1	<0.1	<0.1	<0.1	0.2	0.2	0.3
Zn	20	9	40	18	7	9	23	11	13	19
As	<0.5	<0.5	<0.5	<0.5	0.8	<0.5	1	0.8	<0.5	0.7
Cd	<0.1	<0.1	<0.1	<0.1	<0.1	<0.1	<0.1	<0.1	<0.1	<0.1
Sb	<0.1	<0.1	<0.1	<0.1	<0.1	<0.1	<0.1	<0.1	<0.1	<0.1
Bi	<0.1	<0.1	<0.1	<0.1	<0.1	<0.1	<0.1	<0.1	<0.1	<0.1
Ag	<0.1	<0.1	<0.1	<0.1	<0.1	<0.1	<0.1	<0.1	<0.1	<0.1
Au (ppb)	<0.5	<0.5	0.5	<0.5	<0.5	<0.5	1	1.2	<0.5	1.4
Hg	<0.01	<0.01	<0.01	<0.01	<0.01	<0.01	<0.01	<0.01	<0.01	<0.01
Tl	<0.1	<0.1	0.1	<0.1	<0.1	<0.1	<0.1	<0.1	<0.1	<0.1
Se	<0.5	<0.5	<0.5	<0.5	<0.5	<0.5	<0.5	<0.5	<0.5	<0.5
Σ*REE*	1.12	1.02	2.34	1.22	0.92	1.32	2.06	1.42	1.64	3.36
Σ*LREE*	0.72	0.62	0.82	0.82	0.52	0.92	1.24	0.92	0.62	1.37
Σ*MREE*	0.20	0.20	0.31	0.20	0.20	0.20	0.23	0.20	0.24	0.46
Σ*HREE*	0.10	0.10	0.31	0.10	0.10	0.10	0.19	0.10	0.18	0.33
Eu/Eu*	0.30	0.30	0.30	0.30	0.30	0.30	0.39	0.30	0.31	0.39
Ce/Ce*	0.73	0.52	0.52	0.73	0.31	0.04	1.24	0.73	0.52	1.21

https://doi.org/10.1346/CCMN.2018.064088 Published online by Cambridge University Press

Table 2 (*contd*.)

Major oxides (wt.%)	Asbestos							Claystone		
	BKR-4	GMR-4	KKC3-7	MRZ2-1	BOI-1	OYC-1	Avg.	MRZ2-3	KLR-9	Avg.
SiO_2	36.05	45.47	45.69	57.43	43.99	52.57	43.18	44.41	49.36	46.89
Al_2O_3	0.21	0.38	0.1	0.51	0.81	2.52	1.01	14.52	5.41	9.97
ΣFe_2O_3	5.24	1.74	4.67	3.66	4.31	4.99	5.54	6.72	3.34	5.03
MgO	34.67	36.57	35.19	22.54	19.36	17.73	32.56	16.39	19.38	17.89
CaO	0.45	0.77	0.21	10.46	14.34	13.07	2.9	8.01	8.72	8.37
Na_2O	0.02	<0.01	<0.01	0.04	0.03	0.31	<0.03	1.92	0.11	1.02
K_2O	0.01	<0.01	<0.01	<0.01	<0.01	0.4	<0.03	0.11	0.18	0.15
TiO_2	<0.01	<0.01	<0.01	0.02	0.02	0.3	<0.03	0.24	0.53	0.39
P_2O_5	<0.01	<0.01	<0.01	<0.01	<0.01	0.06	<0.01	<0.01	0.07	<0.04
MnO	0.06	0.07	0.06	0.1	0.12	0.09	0.11	0.13	0.16	0.15
Cr_2O_3	0.181	0.034	0.014	0.027	0.137	0.131	0.2	0.09	0.025	0.058
LOI	22.3	14.3	13.4	4.7	16.5	7.5	13.8	7.1	12.4	9.75
Total	99.42	99.39	99.43	99.63	99.67	99.69	99.49	99.67	99.64	99.66
Trace elements (ppm)										
Ni	1946	660	965	682	453	510	1049	452	166	309
Cr	1238	233	96	185	937	896	1335	616	171	394
Sc	3	<1	5	1	9	7	<5.6	24	9	17
Ba	5	3	2	<1	<1	34	<5.4	8	24	16
Be	5	<1	<1	<1	<1	<1	<1.3	<1	<1	<1
Co	93	76.1	56.9	25.1	50.8	42.9	69.7	60.1	23	41.6
Cs	0.1	<0.1	<0.1	<0.1	<0.1	0.8	<0.1	<0.1	4.5	<2.3
Ga	<0.5	1.6	<0.5	<0.5	1.4	4.9	<1.5	9.4	6.2	7.8
Hf	<0.1	<0.1	<0.1	<0.1	<0.1	0.8	<0.1	0.3	1.3	0.8
Nb	0.2	<0.1	<0.1	0.6	<0.1	4.5	<0.5	0.5	3	1.8
Rb	0.4	<0.1	<0.1	<0.1	<0.1	12.3	<0.9	0.7	18.8	9.8
Sn	<1	<1	<1	<1	<1	<1	<1	<1	<1	<1
Sr	12.2	67.9	4.3	5.5	20.7	38.7	24.8	199.7	83	141.4
Ta	0.1	<0.1	<0.1	<0.1	<0.1	0.3	<0.1	<0.1	0.2	<0.2
Th	<0.2	<0.2	<0.2	<0.2	<0.2	1.9	<0.3	<0.2	0.2	<0.2
U	<0.1	0.2	<0.1	<0.1	0.1	0.6	<0.3	<0.1	0.1	<0.1
V	13	21	<8	19	71	43	<43	112	76	94
W	<0.5	<0.5	<0.5	<0.5	<0.5	<0.5	<0.6	<0.5	<0.5	<0.5
Zr	0.9	0.2	1.5	0.9	1.4	34.1	2.7	10.4	54.7	32.6
Y	0.2	0.4	<0.1	0.7	0.8	4	<0.7	6.1	10.1	8.1
La	0.4	1.8	0.1	0.4	0.3	3.5	0.5	0.6	3.5	2.1
Ce	0.5	2	<0.1	0.4	0.1	7.6	<0.8	1.3	9.1	5.2
Pr	0.04	0.15	<0.02	0.18	<0.02	0.89	<0.1	0.24	1.31	0.78
Nd	<0.3	0.6	<0.3	<0.3	<0.3	4	<0.5	1.3	5.8	3.6
Sm	<0.05	0.11	<0.05	<0.05	<0.05	0.87	<0.1	0.53	1.55	1.04
Eu	<0.02	0.14	<0.02	0.02	<0.02	0.25	<0.04	0.29	0.72	0.51
Gd	<0.05	0.07	<0.05	0.07	0.08	0.9	<0.1	0.85	1.79	1.32
Tb	0.01	<0.01	<0.01	<0.01	0.01	0.14	<0.02	0.16	0.29	0.23
Dy	<0.05	0.07	<0.05	0.1	0.14	0.87	<0.13	1.09	1.86	1.48
Ho	<0.02	<0.02	<0.02	<0.02	0.03	0.14	<0.03	0.24	0.35	0.30
Er	<0.03	<0.03	<0.03	0.07	0.08	0.45	<0.09	0.7	1.07	0.89
Tm	<0.01	<0.01	<0.01	<0.01	0.01	0.06	<0.02	0.1	0.15	0.13
Yb	<0.05	<0.05	<0.05	0.07	0.1	0.43	<0.1	0.63	0.89	0.76
Lu	<0.01	<0.01	<0.01	<0.01	0.01	0.06	<0.02	0.09	0.14	0.12
TOT/C	3.23	0.33	0.14	0.06	3.17	0.96	0.85	0.03	0.55	0.29
TOT/S	0.06	<0.02	<0.02	<0.02	<0.02	<0.02	<0.02	0.06	<0.02	<0.04
Mo	0.1	<0.1	0.1	<0.1	<0.1	<0.1	<0.1	<0.1	<0.1	<0.1
Cu	2	2.1	1.2	23.9	5.0	26.9	9.2	114	111.9	113
Pb	0.5	0.2	0.5	<0.1	0.2	0.4	0.2	0.1	0.6	0.4
Zn	19	12	17	9	13	20	20	35	14	25
As	8.2	<0.5	0.9	<0.5	20.1	1	<2.2	<0.5	7.1	<3.8
Cd	<0.1	<0.1	<0.1	<0.1	<0.1	<0.1	<0.1	<0.1	<0.1	<0.1
Sb	<0.1	<0.1	<0.1	<0.1	<0.1	<0.1	<0.1	<0.1	<0.1	<0.1
Bi	<0.1	<0.1	<0.1	<0.1	<0.1	<0.1	<0.1	<0.1	<0.1	<0.1
Ag	<0.1	<0.1	<0.1	<0.1	<0.1	<0.1	<0.1	<0.1	<0.1	<0.1
Au (ppb)	0.6	<0.5	<0.5	1	1	<0.5	<0.9	<0.5	1.7	<1.1
Hg	<0.01	<0.01	0.01	<0.01	<0.01	<0.01	<0.01	<0.01	<0.01	<0.01
Tl	<0.1	<0.1	<0.1	<0.1	<0.1	<0.1	<0.1	<0.1	<0.1	<0.1
Se	<0.5	<0.5	<0.5	<0.5	<0.5	<0.5	<0.5	<0.5	<0.5	<0.5
Σ*REE*	1.74	5.47	0.92	2.41	2.05	24.6	3.3	14.22	38.62	26.42
Σ*LREE*	1.24	4.55	0.52	1.28	0.72	15.99	1.93	3.44	19.71	11.58
Σ*MREE*	0.20	0.42	0.20	0.27	0.33	3.17	0.43	3.16	6.56	4.86
Σ*HREE*	0.10	0.10	0.10	0.16	0.20	1.00	0.2	1.52	2.25	1.89
Eu/Eu*	0.31	0.57	0.30	0.30	0.30	5.04	0.59	3.73	9.33	6.53
Ce/Ce*	1.05	4.58	0.31	1.78	0.73	12.06	1.64	2.52	14.27	8.40

https://doi.org/10.1346/CCMN.2018.064088 Published online by Cambridge University Press

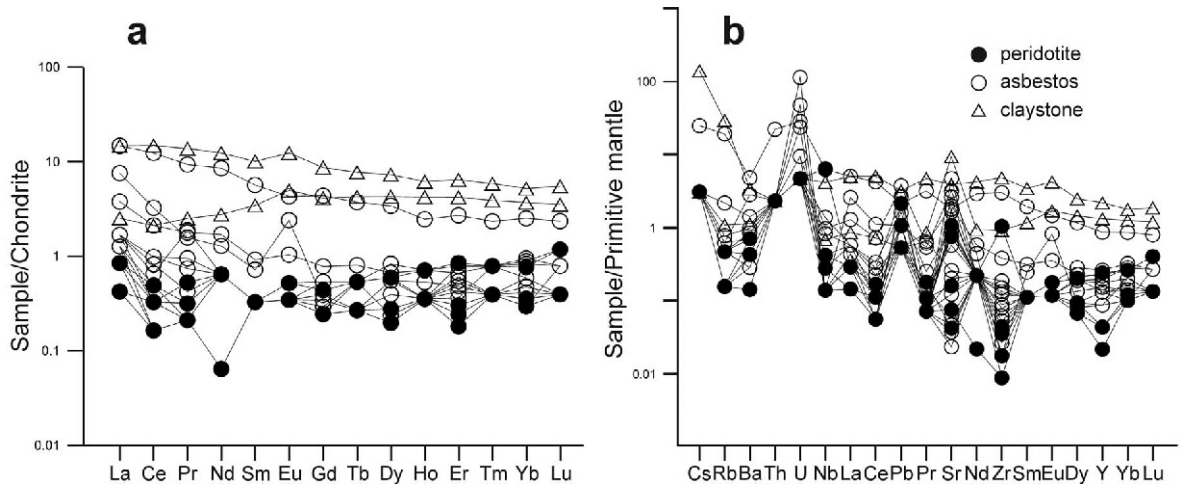

Figure 7. Graphic illustrations of (a) Chondrite and (b) Primitive mantle-normalized patterns for serpentine samples from the Çankırı and Ankara regions (Sun and McDonough, 1989).

given in Table 5 and plotted in Figure 9. The δD and $\delta^{18}O$ values ranged between −67.20 to −133.20‰ for chrysotile and −12.23 to 8.26‰ for chrysotile+tremolite. The chrysotile formation temperatures were calculated to be between 170 and 555ºC using the Saccocia *et al.* (2009) water/serpentitne O-isotopic fractionation factor in the equation: $1000 \ln \alpha = 3.49(10^6/T^2) - 9.48$ (Table 5).

Table 3. Mass gains and losses of major oxides (wt.%) and trace elements (ppm) for the asbestos samples based on the isocon analysis diagram (Figure 8; Grant, 1986, 2005).

			Overall volume change (%)	19.29
			Overall mass change (%)	0.00
			Slope	1.00
Sample	Peridotite Avg. (n = 5)	Asbestos Avg. (n = 20)		
Major oxides (wt.%)	Unaltered C^O	Altered C^A	Gain/Loss relative to C_i^O $\Delta C_i/C_i^O$	Gain/Loss in wt.% ΔC_i
SiO_2	39.93	43.18	0.08	3.25
TiO_2	0.02	0.03	0.50	0.01
Al_2O_3	1.33	1.01	-0.24	-0.32
Fe_2O_3	8.20	5.54	-0.32	-2.66
MnO	0.11	0.11	0.00	0.00
MgO	35.93	32.56	-0.09	-3.37
CaO	0.80	2.87	2.59	2.07
Trace elements (ppm)				Gain/Loss in ppm
Sr	9.00	24.80	1.76	15.80
Pb	0.20	0.20	0.00	0.00
Cr	2607.00	1335.00	-0.49	-1272.00
Ni	2050.00	1049.00	-0.49	-1001.00
Zr	2.60	2.70	0.04	0.10
Y	0.40	0.70	0.75	0.30
Nb	1.10	0.50	-0.55	-0.60
Th	0.20	0.30	0.50	0.10
La	0.10	0.50	4.00	0.40
Pr	0.03	0.10	2.33	0.07
Nd	0.30	0.50	0.67	0.20
Sm	0.05	0.10	1.00	0.05

n = number of samples.

https://doi.org/10.1346/CCMN.2018.064088 Published online by Cambridge University Press

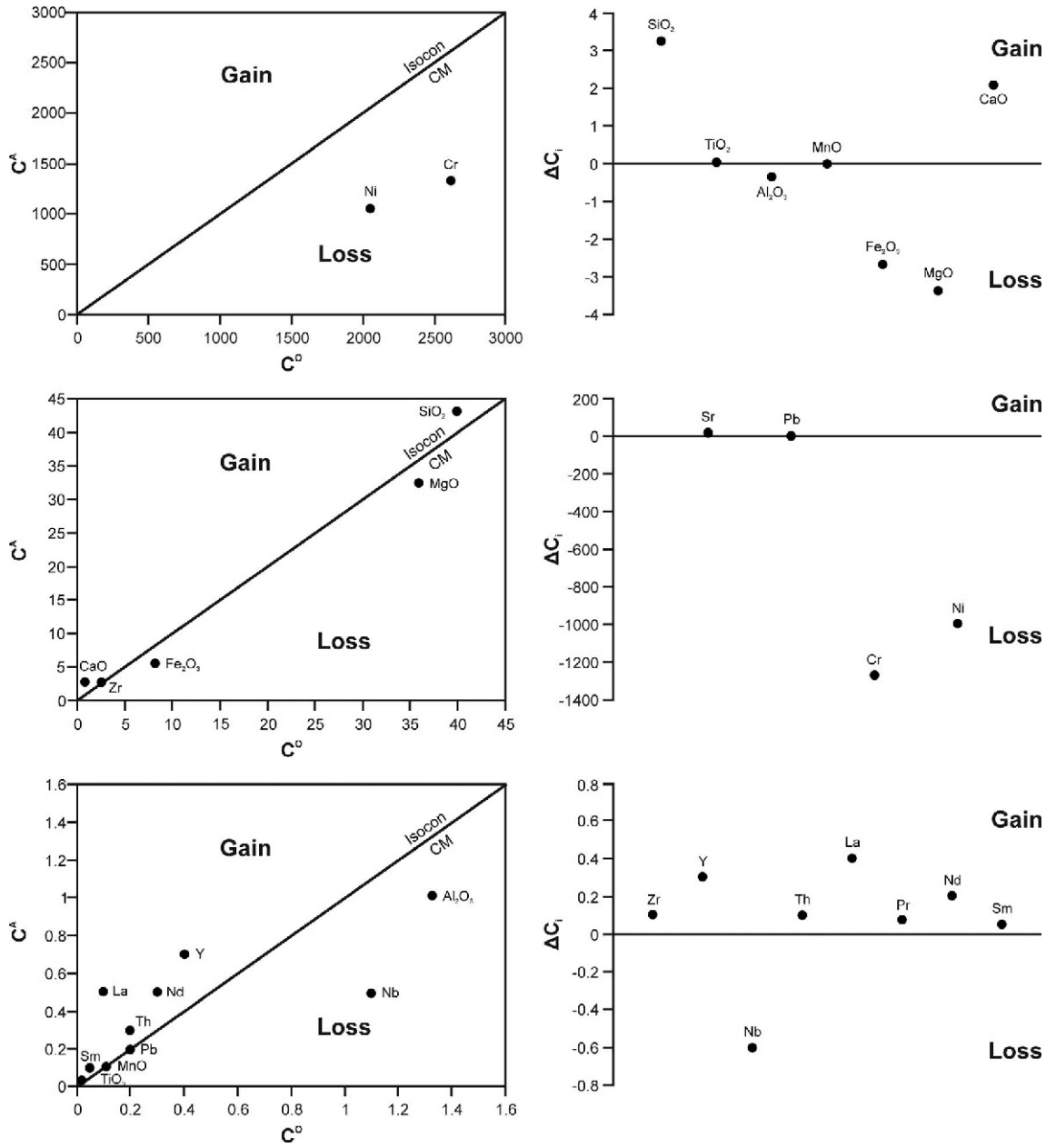

Figure 8. Mass changes in the major elements (in grams) and trace elements (in ppm) for the asbestos samples from the Çankırı and Ankara regions based on the isocon analysis diagram (Grant, 1986, 2005; López-Moro, 2012). The CM lines indicate a constant mass with no gains or losses.

DISCUSSION

Mineralogy and geochemistry

Chrysotile and localized tremolite occur in widely exposed dunite-harzburgite and pyroxenite units in the Çankırı and Ankara regions. Chrysotile and tremolite formed as a result of hydrothermal alteration plus/minus chemical weathering along multiple tectonic deformation zones of the dunite-harzburgite and pyroxenite units. A white to pale green, fibrous chrysotile+tremolite layer that was 0.5–10 cm long and 1–3 mm thick developed as a blanket on serpentinized dunite-harzburgite, pyroxenite, and fracture in-fill. Abundant chrysotile and tremolite deposits associated with ophiolitic units in the USA and Italy were reported by Pacella *et al.* (2010). In contrast, abundant tremolite that formed in altered metamorphics and chrysotile that formed in the serpentinized ophiolitic units along the tectonic zone was affected by hydrothermal alteration in the Eskişehir region (Kadir and Erkoyun, 2015). The white to green color of the chrysotile asbestos minerals and the absence

https://doi.org/10.1346/CCMN.2018.064088 Published online by Cambridge University Press

Table 4. Chemical compositions (wt.%) and structural formulae of chrysotile and tremolite obtained from ATEM analyses.

	Chrysotile					
Major oxide (wt.%)	DLL-1 (1)	DLL-1 (9)	DLL-1 (10)	DLL-1 (11)	DLL-1 (12)	Avg.
SiO_2	47.81	48.40	48.73	48.97	48.52	48.49
Al_2O_3	–	1.70	0.70	1.07	0.74	0.84
ΣFe_2O_3	1.55	1.09	1.89	1.76	1.54	1.57
MgO	46.66	43.93	44.88	44.86	47.55	45.58
CaO	0.16	0.28	0.06	0.13	0.17	0.16
Na_2O	3.30	4.04	3.30	2.90	1.24	2.96
K_2O	0.52	0.5	0.37	0.30	0.23	0.38
MnO	–	0.06	0.07	–	–	0.03
Total	100.00	100.00	100.00	100.00	100.00	100.00
Si	3.92	3.95	3.99	3.99	3.94	3.96
Al	–	0.05	0.01	0.01	0.06	0.03
ΣT	3.92	4.00	4.00	4.00	4.00	3.99
Al	–	0.11	0.05	0.09	0.01	0.05
Fe^{3+}	0.09	0.06	0.1	0.1	0.09	0.09
Mg	5.70	5.35	5.47	5.45	5.75	5.54
Mn	–	0.003	0.004	–	–	0.001
Ca	0.01	0.02	0.004	0.009	0.01	0.01
ΣC	5.80	5.54	5.62	5.65	5.86	5.69
Na	0.52	0.69	0.4	0.39	0.19	0.44
K	0.05	0.04	0.02	0.03	0.01	0.03
ΣA	0.57	0.73	0.42	0.42	0.2	0.47

	Tremolite				
Major oxide (wt.%)	AHL-3 (5)	AHL-3 (18)	CPR-3 (6)	CPR-3 (10)	Avg.
SiO_2	54.20	55.30	56.06	55.84	55.35
Al_2O_3	0.50	0.34	0.57	0.91	0.58
ΣFe_2O_3	4.50	2.19	2.27	3.73	3.17
MgO	23.86	23.40	23.82	21.78	23.21
CaO	11.20	8.99	10.83	10.78	10.45
Na_2O	0.40	1.22	0.74	0.30	0.66
K_2O	0.26	0.82	0.31	0.26	0.41
MnO	0.06	–	–	–	0.01
Total	99.60	98.60	99.61	99.16	99.24
Si	7.69	7.95	7.88	7.93	7.86
Al	0.08	0.05	0.1	0.15	0.1
Fe^{3+}	0.23	–	0.02	–	0.06
ΣT	8.00	8.00	8.00	8.08	8.02
Fe^{3+}	0.24	0.24	0.22	0.40	0.28
Mg	4.76	4.76	4.78	4.6	4.72
ΣC	5.00	5.00	5.00	5.00	5.00
Mg	0.28	0.25	0.21	0.01	0.19
Mn	0.007	–	–	–	0.002
Ca	1.70	1.38	1.63	1.63	1.59
ΣB	1.99	1.63	1.84	1.64	1.78
Na	0.1	0.33	0.19	0.07	0.17
K	0.05	0.14	0.05	0.03	0.07
ΣA	0.15	0.47	0.24	0.10	0.24

The numbers in parentheses indicate the microchemical analysis numbers for different individual chrysotile and tremolite fibers in each sample.

https://doi.org/10.1346/CCMN.2018.064088 Published online by Cambridge University Press

Table 5. Oxygen and hydrogen isotopic compositions of chrysotile (Ctl) and chrysotile + tremolite (Ctl + Tr) from the Çankırı and Ankara regions with the calculated formation temperatures.

Sample	Mineralogy	Weight (mg)	%H	Normalized δ^2H vs. VSMOW	%O	Normalized $\delta^{18}O$ vs. VSMOW	Formation temperature* (ºC)
AHL-1	Ctl	1.57	1.53	−106.17	11.63	1.23	297
ASR3-1	Ctl	1.54	1.42	−102.68	14.16	7.24	183
KTK1-1	Ctl	1.49	1.43	−101.62	12.79	8.26	170
GMR-4	Ctl	1.53	1.55	−119.27	11.64	−1.15	374
KKC3-7	Ctl	1.53	1.50	−133.20	11.62	0.61	315
DMT-6	Ctl	1.47	1.52	−129.21	13.08	4.35	229
KLC-2	Ctl	1.51	1.56	−124.14	12.41	1.28	296
GDR-1	Ctl	1.51	1.41	−67.20	11.73	−0.75	359
KLR-8	Ctl	1.49	1.45	−57.17	11.15	−12.23	–
DLL-1	Ctl	1.50	1.45	−78.85	12.83	−4.40	555
YYC-4	Ctl + Tr	1.53	1.47	−77.67	11.43	−6.83	–
AVC-1	Ctl + Tr	1.52	1.42	−77.26	11.00	−2.90	455

* Formation temperatures of chrysotile were calculated assuming $\delta^{18}O_{water}$ = 0.00‰ (Zheng, 1993).

of red and brown asbestos suggests the influence of chemical weathering/hydrothermal alteration along tectonic deformation zones in the Çankırı and Ankara regions. The absence of metamorphic deformation is similar to that reported for the Cana Brava (Brazil) locality by Biondi (2014).

The development of bundles, knitted aggregates, or a mesh of chrysotile/tremolite on relict olivine, pyroxene (enstatite-augite), and Fe-(oxyhydr)oxide plus the presence of enclosing silica-filling veins with non-pseudomorphic textures suggest *in situ* formation during hydrothermal alteration of dunite-harzburgite and pyroxenite. The absence of brucite, antigorite, and talc in association with chrysotile/tremolite suggest formation under a high pressure and temperature regime (Wicks and Whittaker, 1977) that was possibly related to the subduction-accretion mechanism of the upper mantle and/or overthrusting during the latest Cretaceous through the early Cenozoic (Sarıfakıoğlu *et al.*, 2017).

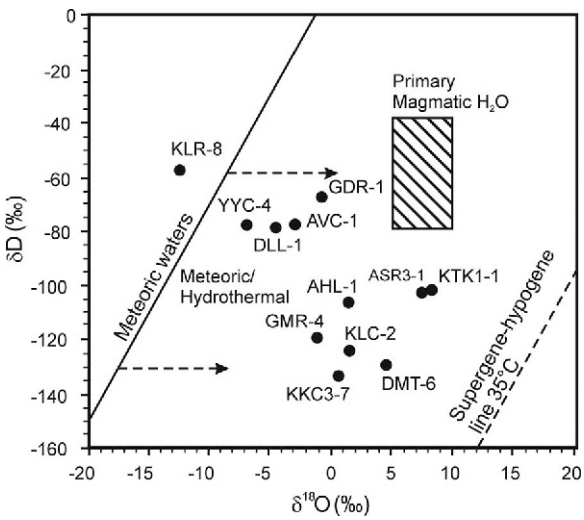

Figure 9. $\delta^{18}O$ vs. δD plot showing isotopic compositions of asbestos samples from the Çankırı and Ankara regions (Savin and Epstein, 1970). The supergene/hypogene kaolinite equilibrium line with meteoric water at 35ºC is from Sheppard *et al.* (1969). The meteoric water line is from Craig (1961).

The sharp diagnostic XRD reflections of fibrous chrysotile and tremolite with regular outlines suggests these minerals are well crystallized (Brindley, 1980b; Zaremba *et al.*, 2010). From chemical analyses, the average structural formulae for chrysotile and tremolite are calculated to be:

$(Na_{0.44}K_{0.03})(Mg_{5.54}Fe_{0.09}Al_{0.05}Ca_{0.01}Mn_{0.001})(Si_{3.96}Al_{0.03})O_{10}(OH)_8$ and $(Na_{0.17}K_{0.07})(Ca_{1.59}Mg_{0.19}Mn_{0.002})(Mg_{4.72}Fe_{0.28})(Si_{7.86}Al_{0.1}Fe_{0.06})O_{22}(OH)_2$, respectively.

The mass loss of MgO, Fe_2O_3, Al_2O_3, Ni, Cr, and Nb and gain of SiO_2, TiO_2, CaO, Zr, Y, Th, La, Sr, Pr, Nd, and Sm based on the isocons reflect fractionation of olivine and pyroxene during serpentinization of peridotite, which is similar to that reported by Beinlich *et al.* (2010) and Jöns *et al.* (2010). The slightly leached MgO, Fe_2O_3, and Al_2O_3 values suggest these elements were possibly fixed in the structure of brucite/hydromagnesite, magnetite, and smectite/chlorite crystals that were in or out of the serpentinized zone.

The enrichment of *LREE* relative to *HREE* in the dunite-harzburgite and pyroxenite asbestos samples according to chondrite-normalized patterns suggests that the concentration of *LREE* was due to olivine and pyroxene fractionation under hydrothermal conditions (Niu, 2004; Khedr and Arai, 2009). In addition, enrichment of *LREE* and the negative Eu anomaly in chrysotile (avg. 0.36) and related pyroxenite and dunite-harzburgite (avg. 0.32) samples may be a consequence of the serpentinization and the associated increased solu-

https://doi.org/10.1346/CCMN.2018.064088 Published online by Cambridge University Press

tion/rock interactions (Niu, 2004; Paulick *et al*., 2006). The positive Ce anomaly in asbestos may be a result of the oxidation of Fe in ferromagnesian minerals, such as pyroxene, during serpentinization (Barnes *et al*., 2013). The positive Ce anomaly in the claystone samples may suggest a lateritic weathering environment (Marsh, 1991; González-Álvarez *et al*., 2013).

The depletion of Rb, Ba, Ce, Pr, Sr, Zr, and Y relative to the primitive mantle and the range in the chrysotile formation temperature (170−555ºC) calculated from the isotope data also suggest that chrysotile/tremolite formed as a result of a tectonically controlled hydrothermal process during serpentinization (Sheppard and Gilg, 1996; Gilg *et al*., 2003; Kadir and Erkoyun, 2015). A similar high temperature range for the serpentinization of olivine and pyroxene in an accretionary tectonic setting during ophiolite emplacement was described by Coleman (1977) and Früh-Green *et al.* (1990). The association of hydromagnesite with mainly chrysotile, locally with tremolite, and/or with chrysotile+tremolite is also consistent with high temperature ±135ºC serpentinization similar to that reported by Knupp (1999). This interpretation is consistent with the positive $\delta^{18}O$ values for the late-stage chrysotile and silica fracture filling and the negative $\delta^{18}O$ values that are related to earlier formed chrysotile (Nuriel *et al*., 2009). The negative δD values in chrysotile/tremolite may reflect hydrogen isotopic exchange in meteoric waters subsequent to precipitation.

Genetic model

Chrysotile and tremolite may form by the alteration of precursor minerals, such as olivine and/or pyroxene, as a result of an intra-oceanic subduction-accretion or/and following uplifting of upper mantle peridotites through thrust faulting that is locally associated with silica fracture-infill derived from hydrothermal water (Wenner and Taylor, 1973; Van Gosen, 2007; Iyer *et al.*, 2008; Lafay *et al.*, 2012; Malvoisin and Brunet, 2014).

Texturally and micromorphologically, dissolution and fractures at the cleavage boundaries of precursor olivine and pyroxene crystals together with the outward increase of knitted aggregate/fiber bundles of chrysotile/tremolite from the precursor crystal margins suggests a dissolution-precipitation mechanism (Figures 10a, 10b). Furthermore, development of silica-filling micro-veins in fractured olivine and the association of tremolite bundle fibers with spherical opal-CT may be a consequence of silica release during degradation of olivine and/or pyroxene. Field observations plus mineralogical and geochemical data demonstrate that chrysotile and tremolite have formed by the following two processes. Firstly, the reaction of hydrothermal fluid with olivine and pyroxene crystals in dunite-harzburgite and pyroxenite resulted in the formation of chrysotile and tremolite, respectively. This reaction mechanism for hydrothermal fluid with olivine crystals and chrysotile, magnetite, and hydromagnesite formation can be summarized as follows (equations 1, 2, 3; Figure 10a; Moody, 1976; Iyer, 2007; Montes-Hernandez *et al.*, 2012):

$$\underset{\text{Forsterite}}{(FeMg)_2SiO_4} + H_2O \rightarrow \underset{\text{Chrysotile}}{Mg_3Si_2O_6(OH)_2} + \underset{\text{Brucite}}{Mg(OH)_2} + \underset{\text{Ferroan brucite}}{2Fe(OH)_2} \quad (1)$$

$$\underset{\text{Ferroan brucite}}{3Fe(OH)_2} \rightarrow \underset{\text{Magnetite}}{Fe_3O_4} + H_2 + 2H_2O \quad (2)$$

$$\underset{\text{Brucite}}{Mg(OH)_2} + 0.8CO_2 \rightarrow \underset{\text{Hydromagnesite}}{0.2Mg_5(CO_3)_4(OH)_2.4H_2O} \quad (3)$$

The second mechanism is the reaction of hydrothermal fluid with both augite and enstatite crystals or with forsterite+augite and the formation of tremolite can be written as follows (equations 4, 5; Figure 10b; Jenkins, 1987):

$$\underset{\text{Augite}}{(CaNa)(MgFeAl)(AlSi)_2O_6} + \underset{\text{Enstatite}}{(FeMg)SiO_3} + SiO_2 + H_2O \rightarrow \underset{\text{Tremolite}}{Ca_2Mg_5Si_8O_{22}(OH)_2} \quad (4)$$

$$\underset{\text{Forsterite}}{(FeMg)_2SiO_4} + \underset{\text{Augite}}{(CaNa)(MgFeAl)(AlSi)_2O_6} + H_2O \rightarrow \underset{\text{Tremolite}}{Ca_2Mg_5Si_8O_{22}(OH)_2} \quad (5)$$

The lack of brucite and talc in association with chrysotile/tremolite may be due to the open hydrological system that leached excess Mg and Fe (Sonzogni *et al.*, 2017). Magnesium and Fe may also be consumed in the formation of hydromagnesite and magnetite. Mumpton and Thompton (1975), however, reported that brucite is unstable and can be altered to hydromagnesite under chemical weathering. Montes-Hernandez *et al.* (2012) experimentally found that hydromagnesite forms from brucite and CO_2 under high temperature and pressure conditions that reflect the absence of Na-rich seawater during or following serpentinization. The absence of chloride, sulfate, and calcite minerals in association with the asbestos minerals is further evidence that the asbestos minerals do not have a seawater origin and that these minerals formed under low salinity conditions (Sonzogni *et al*., 2017).

Environmental effect of asbestos

The total number of villagers exposed to asbestos fibers in rural areas of the Çankırı and Ankara provinces were 3046 and 1307, respectively (Metintaş *et al*., 2017). Malignant mesothelioma cases mostly occur in the Gümerdiğin, Gürpınar, and Çapar villages of the Çankırı region and around the Beynam, Oyaca, Haymana Yukarıyapançarşak, and Akçavirançarşak areas in the Ankara region (Barış, 1987, 1994, 2003,

https://doi.org/10.1346/CCMN.2018.064088 Published online by Cambridge University Press

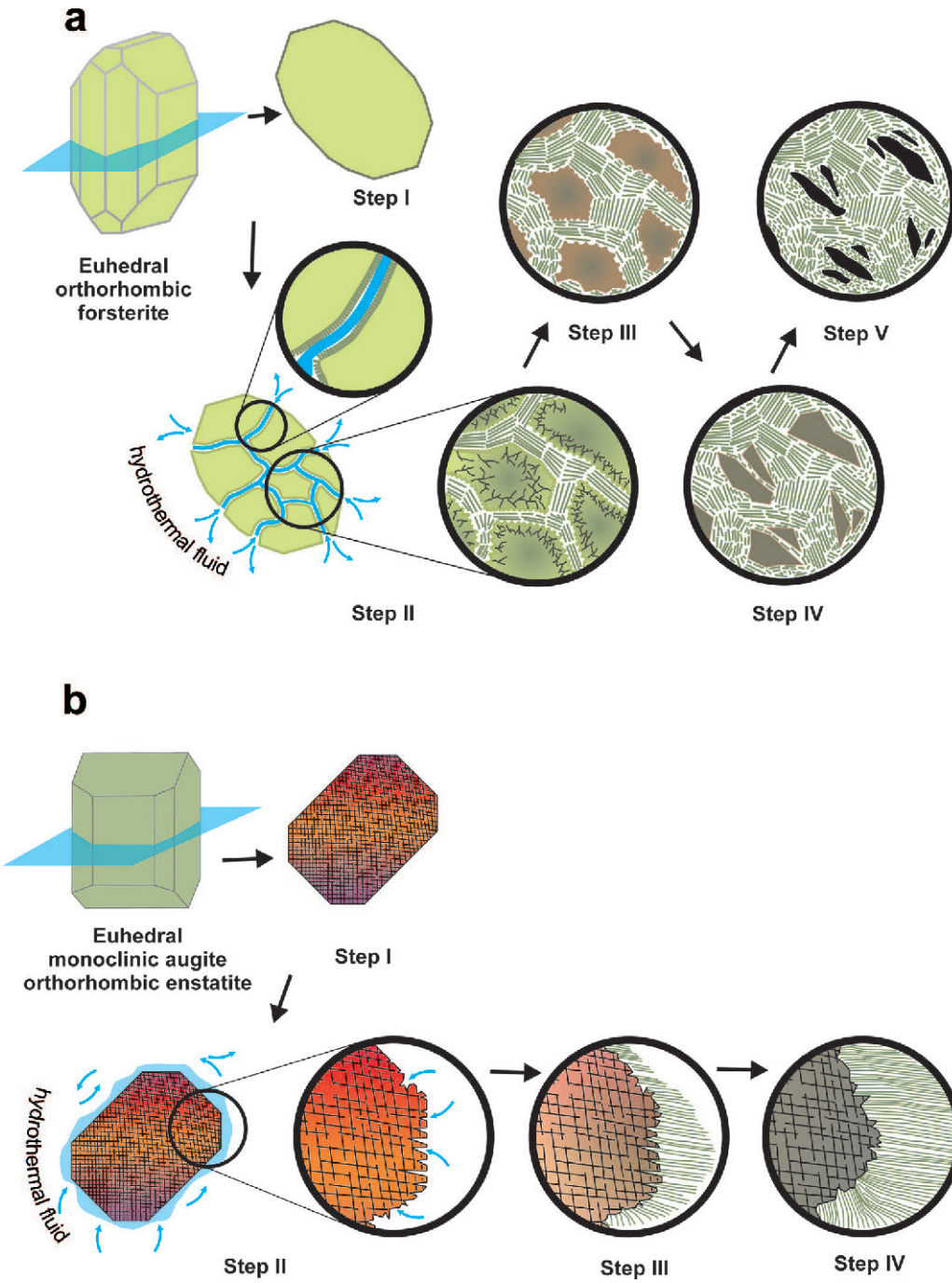

Figure 10. Schematic synthesis diagram for the formation of (a) chrysotile and (b) tremolite fibers from the degradation of olivine and pyroxene, respectively.

2008; Barış and Atabey, 2009). Eighteen mesothelioma cases have been diagnosed in the Çankırı region, 20 cases in Gürpınar village, and anonymous asbestos contact mesothelioma cases in other villages of the Çankırı and Ankara regions (Barış, 1987, 2003). The risk ratio for malignant mesothelioma in the Çankırı (6.45) region is lower than in the Eskişehir region (9.08) (Metintaş *et al*., 2017). These data are consistent with the slightly lower number of statistically estimated malignant mesothelioma cases in the Çankırı and Ankara regions relative to the Eskişehir region where 48 rural areas are exposed to asbestos fibers (Turkish Mesothelioma Working Group, 2015; Kadir and Erkoyun, 2015). This decrease correlates with a decrease in tremolite abundance in comparison to chrysotile asbestos occurrences and the decreased number of total

https://doi.org/10.1346/CCMN.2018.064088 Published online by Cambridge University Press

rural areas affected in the Çankırı and Ankara regions in comparison to Eskişehir.

CONCLUSIONS

Chrysotile- and localized chrysotile+tremolite-rich asbestos materials are widely exposed in the Çankırı and Ankara regions of central Anatolia, Turkey. These materials occur on fracture surfaces in tectonic deformation zones and in altered Cretaceous dunite-harzburgite and pyroxenite rocks. Serpentinization of these units resulted in the formation of tremolite/chrysotile with non-pseudomorphic textures and hydromagnesite. Development of bundled or knitted/mesh chrysotile and tremolite in association with relict olivine/pyroxene and Fe-(oxyhydr)oxide indicate tectonically controlled *in situ* formation. The depletion of MgO, Fe_2O_3, Al_2O_3, Ni, Cr, Nb, and *HREE* relative to the *LREE* ratio and the negative Eu anomaly suggest fractionation of metastable olivine and pyroxene and the consequent formation of chrysotile and tremolite where hydrothermal fluids occurred during accretion and/or uplift of ophiolitic units of the region and in a high temperature and pressure regime. The $\delta^{18}O$ and δD value plots for chrysotile and chrysotile+tremolite between the supergene/hypogene water line, the meteoric water line, and the primary magmatic water area plus the calculated crysotile/tremolite formation temperature of 170−555ºC suggest the influence of hydrothermal processes.

The concentrations of tremolite associated with chrysotile in asbestos materials is an important factor in the development of malignant mesothelioma cases in the Çankırı and Ankara regions and was demonstrated by the geographic correlation between tremolite, chrysotile, and malignant mesothelioma.

ACKNOWLEDGMENTS

This present study was supported financially by the Scientific Research Projects Fund of Eskişehir Osmangazi University in the framework of Project 2014−656. The authors are indebted to the editors and to the anonymous reviewers for their extremely careful and constructive reviews which improved the quality of the paper significantly. This paper was presented at the 16th International Clay Conference 2017, held at Granada, Spain. Nergis Önalgil is thanked for assisting during the field work.

REFERENCES

Atabey, E. (2009) Türkiye'de asbest, eriyonit, kuvars ve diğer mineral tozları ve etkileri. *MTA Yer Bilimleri ve Kültür Serisi*, **6**, 191s.

Atabey, E. (2015) Türkiye asbest haritası (çevresel asbest maruziyeti-akciğer kanseri-mezotelyoma). *Tüberküloz ve Toraks Dergisi*, **63**, 199−219.

Atabey, E. and Ünal, H. (2008) Batı Anadolu'daki Jeolojik Unsurlar ve Halk Sağlığı Projesi Tıbbi Jeoloji Raporu, MTA Rapor No. 11067.

Barış, Y.İ. (1987) *Asbestos and Erionite Related Chest Diseases*. Semih Ofset Matbaası, Ankara, Turkey, 167 pp.

Barış, Y.İ. (1994) *Bu Doktoru Rehin Alalım: Anadolu'da bir Kanser Arastırması*. Ajans Türk Mat. San. A.S., Kent Matbaası, Ankara, Turkey, 112 pp.

Barış, Y.İ. (2003) *İğdeköy / Emet-Kütahya Ara*ştırması, Asbest'ten Sonra Arsenik, Anadolu'nun Bitmeyen Akciğer ve Karın Zarı Kanseri Çilesi. Bilimsel Tıp Yayınevi, Ankara, Turkey, 72−80 pp.

Barış, Y.İ. (2008) Türkiye'de asbest ve eriyonit sorunu. *Uluslararası Katılımlı Tıbbi Jeoloji Sempozyum Kitabı* (Eşref Atabey, editor), 18, YMGV Yayını, ISSN: 978-975-7946-33-5.İstanbul, Turkey.

Barış, Y.İ. and Atabey, E. (2009) *Türkiye'de Mesleksel ve Çevresel Hastalıklar, Köseleciler 1933*, Magic Digital Center, Bursa, 221 pp.

Barnes, J.D., Eldam, R., Lee, C.-T.A., Errico, J.C., Loewy, S., and Cisneros, M. (2013) Petrogenesis of serpentinites from the Franciscan Complex, western California, USA. *Lithos*, **178**, 143−157.

Bau, M. and Dulski, P. (1996) Distribution of yttrium and rare-earth elements in the Penge and Kuruman iron-formations, Transvaal Supergroup, South Africa. *Precambrian Research*, **79**, 37−55.

Bayram, M., Döngel, I., Bakan, N.D., Yalçın, H., Cevit, R., Dumortier, P., and Nemery, B. (2013) High risk of malignant mesothelioma and pleural plaques in subjects born close to ophiolites. *Chest*, **143**, 164−171.

Beinlich, A., Austrheim, H., Glodny, J., Erambert, M., and Andersen, T.B. (2010) CO_2 sequestration and extreme Mg depletion in serpentinized peridotite clasts from the Devonian Solund Basin, SW Norway. *Geochimica Cosmochimica Acta*, **74**, 6935−6964.

Biondi, J.C. (2014) Neoproterozoic Cana Brava chrysotile deposit (Goiás, Brazil): Geology and geochemistry of chrysotile vein formation. *Lithos*, **184−187**, 132−154.

Brindley, G.W. (1980a) Quantitative X-ray analysis of clays. pp. 411−438 in: *Crystal Structures of Clay Minerals and Their X-ray Identification* (G.W. Brindley and G. Brown, editors) Mineralogical Society Monograph **5**, London.

Brindley, G.W. (1980b) Order−disorder in clay mineral structures. Pp. 125−196 in: *Crystal Structures of Clay Minerals and Their X-ray Identification* (G.W. Brindley and G. Brown, editors). Mineralogical Society Monograph **5**, London.

Çelik, Ö.F., Marzoli, A., Marschik, R., Chiaradia, M., Neubauer, F., and Öz, İ. (2011) Early-Middle Jurassic intra-oceanic subduction in the İzmir−Ankara−Erzincan Ocean, Northern Turkey. *Tectonophysics*, **509**, 120−134.

Çelik, Ö.F., Chiaradia, M., Marzoli, A., Billor, Z., and Marschik, R. (2013) The Eldivan Ophiolite and volcanic rocks in the İzmir−Ankara−Erzincan suture zone, Northern Turkey: Geochronology, whole-rock geochemical and Nd-Sr-Pb isotope characteristics. *Lithos*, **172-173**, 31−46.

Coleman, R.G. (1977) Emplacement and metamorphism of ophiolites. *Rendiconti Società Italiana di Mineralogia e Petrologia*, **33**, 161−190.

Craig, H. (1961) Isotopic variations in meteoric waters. *Science*, **133**, 1702−1703.

Dai, S., Graham, I.T., and Ward, C.R. (2016) A review of anomalous rare earth elements and yttrium in coal. *International Journal of Coal Geology*, **159**, 82−95.

Dangerfield, A., Harris, R., Sarıfakıoğlu, E., and Dilek, Y. (2011) Tectonic evolution of the Ankara Mélange and associated Eldivan ophiolite near Hançili, central Turkey. Pp. 143−169 in: *Mélanges: Processes of Formation and Societal Significance* (J. Wakabayashi and Y. Dilek, editors). The Geological Society of America Special Paper, 480.

Della Ventura, G., Caprilli, E., Bellatreccia, F., De Benedetti, A.A., and Mottana, A. (2014) Asbestiform tremolite within

the Holocene late pyroclastic deposits of Colli Albani volcano (Latium, Italy): Occurrence and crystal chemistry. *Rendiconti Lincei. Scienze Fisiche e Naturali*, **25**, 229–236.

Dilek, Y. and Thy, P. (2006) Age and petrogenesis of plagiogranite intrusions in the Ankara mélange, central Turkey. *Island Arc*, **15**, 44–57.

Döngel, İ., Bayram, M., Bakan, N.D., Yalçın, H., and Gültürk, S. (2013) Is living close to ophiolites related to asbestos related diseases? Cross-sectional study. *Respiratory Medicine*, **107**, 870–874.

Evans, B.W., Ghiorso, M.S., and Kuehner, S.M. (2000) Thermodynamic properties of tremolite: A correction and some comments. *American Mineralogist*, **85**, 466–472.

Foresti, E., Fornero, E., Lesci, I.G., Rinaudo, C., Zuccheri, T., and Roveri, N. (2009) Asbestos health hazard: A spectroscopic study of synthetic geoinspired Fe-doped chrysotile. *Journal of Hazardous Materials*, **167**, 1070–1079.

Früh-Green, G.L., Weissert, H., and Bernoulli, D. (1990) A multiple fluid history recorded in Alpine ophiolites. *Journal of the Geological Society*, **147**, 959–970.

Gilg, H.A., Weber, B., Kasbohm, J., and Frei, R. (2003) Isotope geochemistry and origin of illite-smectite and kaolinite from the Seilitz and Kemmlitz kaolin deposits, Saxony, Germany. *Clay Minerals*, **38**, 95–112.

González-Álvarez, I., Sweetapple, M., Lindley, I.D., and Kirakar, J. (2013) Hydrothermal Ni: Doriri Creek, Papua New Guinea. *Ore Geology Reviews*, **52**, 37–57.

Gökten, E. and Floyd, P.A. (2007) Stratigraphy and geochemistry of pillow basalts within the ophiolitic mélange of the İzmir–Ankara–Erzincan suture zone: implications for the geotectonic character of the northern branch of Neotethys. *International Journal of Earth Sciences*, **96**, 725–741.

Grant, J.A. (1986) The isocon diagram – A simple solution to Gresens' equation for metasomatic alteration. *Economic Geology*, **81**, 1976–1982.

Grant, J.A. (2005) Isocon analysis: A brief review of the method and applications. *Physics and Chemistry of the Earth*, **30**, 997–1004.

Hakyemez, Y., Barkurt, M.Y., Bilginer, E., Pehlivan, S., Can, B., Dağer, Z., and Sözeri, B. (1986) *Yapraklı-Ilgaz-Çankırı-Çandır dolayının jeolojisi*. MTA Rapor No: 7966, Ankara, Turkey.

Iyer, K. (2007) *Mechanisms of Serpentinization and Some Geochemical Effects*. PhD Thesis, Department of Physics of Geological Processes, Faculty of Mathematics and Natural Sciences, University of Oslo, 36 p.

Iyer, K., Jamtveit, B., Mathiesen, J., Malthe-Sørenssen, A., and Feder, J. (2008) Reaction-assisted hierarchical fracturing during serpentinization. *Earth and Planetary Science Letters*, **267**, 503–516.

Jenkins, D.M. (1987) Synthesis and characterization of tremolite in the system H_2O-CaO-MgO-SiO_2. *American Mineralogist*, **72**, 707–715.

Jöns, N., Bach, W., and Klein, F. (2010) Magmatic influence on reaction paths and element transport during serpentinization. *Chemical Geology*, **274**, 196–211.

Kadir, S., Kolaylı, H., and Eren, M. (2012) Genesis of sedimentary- and vein-type magnesite deposits at Kop Mountain, NE Turkey. *Turkish Journal of Earth Sciences*, **21**, 1–18.

Kadir, S., Aydogan, M.S., Elitok, O., and Helvacı C. (2015) Composition and genesis of nickel–chrome–bearing nontronite and montmorillonite in lateritized ultramafic rocks in the Muratdagi region (Uşak, western Anatolia), Turkey. *Clays and Clay Minerals*, **63**, 163–184.

Kadir, S. and Erkoyun, H. (2015) Characterization and distribution of fibrous tremolite and chrysotile minerals in the Eskisehir region of western Turkey. *Clay Minerals*, **50**, 441–458.

Kadir, S., Külah, T., Önalgil, N., Erkoyun, H., and Elliott, W.C. (2017) Mineralogy, geochemistry, and genesis of bentonites in Miocene volcanic-sedimentary units of the Ankara-Çankırı basin, central Anatolia, Turkey. *Clays and Clay Minerals*, **65**, 64–91.

Karadenizli, L. (2011) Oligocene to Pliocene palaeogeographic evolution of the Çankırı-Çorum Basin, central Anatolia, Turkey. *Sedimentary Geology*, **237**, 1–29.

Kaymakçı, N. (2000) Tectono-stratigraphical evolution of the Çankırı Basin (Central Anatolia, Turkey). *Geologia Ultraiectina*, **190**, 1–247.

Khedr, M.Z. and Arai, S. (2009) Geochemistry of metasomatized peridotites above subducting slab: A case study of hydrous metaperidotites from Happo-O'ne comple, central Japan. *Journal of Mineralogical and Petrological Sciences*, **104**, 313–318.

Knupp, R.L. (1999) *The Origin of Brucite in Hydrothermally Altered Limestone Near Devil Peak, Nevada*. MSc Thesis, Department of Geoscience, University of Nevada, Las Vegas, Nevada, USA 143 p.

Koçyiğit, A. (1987) Hasanoğlan (Ankara) yöresinin tektono-stratigrafisi: Karakaya orojenik kuşağının evrimi. *Hacettepe University Earth Science Bulletin*, **14**, 269–293.

Koçyiğit, A., Türkmenoğlu, A., Beyhan, A., Kaymakçı, N., and Akyol, E. (1995) Post– collisional tectonics of Eskişehir – Ankara – Çankırı Segment of İzmir – Ankara – Erzincan Suture Zone (IAESZ): Ankara orogenic phase. *Turkish Association of Petroleum Geologists Bulletin*, **6**, 69–86.

Kuşçu, İ. and Erler, A. (1998) Mineralization events in a collision-related setting: The Central Anatolian Crystalline Complex, Turkey. *International Geology Review*, **40**, 552–565.

Külah, T., Kadir, S., Gürel, A., Eren, M., and Önalgil, N. (2014) Mineralogy, geochemistry, and genesis of mudstones in the upper Miocene Mustafapaşa member of the Ürgüp formation in the Cappadocia region, central Anatolia, Turkey. *Clays and Clay Minerals*, **62**, 267–285.

Lafay, R., Montes-Hernandez, G., Janots, E., Chiriac, R., Findling, N., and Toche, F. (2012) Mineral replacement rate of olivine by chrysotile and brucite under high alkaline conditions. *Journal of Crystal Growth*, **347**, 62–72.

Lamadrid, H.M., Rimstidt, J.D., Schwarzenbach, E.M., Klein, F., Ulrich, S., Dolocan, A., and Bodnar, R.J. (2017) Effect of water activity on rates of serpentinization of olivine. *Nature Communications*, 8:16107, DOI: 10.1038/ncomms16107.

Lescano, L., Gandini, N.A., Marfil, S.A., and Maiza, P.J. (2015) Biological effects of Argentine asbestos: Mineralogical and morphological characterisation. *Environmental Earth Sciences*, **73**, 3433–3444.

Liu, Y., Deng, J., Shi, G., Yui, T-Fu., Zhang, G., Abuduwayiti, M., Yang, L., and Sun, X. (2011) Geochemistry and petrology of nephrite from Alamas, Xinjiang, NW China. *Journal of Asian Earth Sciences*, **42**, 440–451.

López-Moro, F.J. (2012) EASYGRESGRANT – A Microsoft Excel spreadsheet to quantify volume changes and to perform mass-balance modeling in metasomatic systems. *Computers and Geosciences*, **39**, 191–196.

Malvoisin, B. and Brunet, F. (2014) Water diffusion-transport in a synthetic dunite: Consequences for oceanic peridotite serpentinization. *Earth and Planetary Science Letters*, **403**, 263–272.

Marsh, J.S. (1991) REE fractionation and Ce anomalies in weathered Karoo dolerite. *Chemical Geology*, **90**, 189–194.

Metintaş, M., Özdemir, N., Hillerdal, G., Uçgun, I., Metintaş, S., Baykul, C., Elbek, O., Mutlu, S., and Kolsuz, M. (1999) Environmental asbestos exposure and malignant pleural mesothelioma. *Respiratory Medicine*, **93**, 349–355.

Metintaş, S., Metintaş, M., Ucgun, I., and Oner, U. (2002a) Malignant mesothelioma due to environmental exposure to

asbestos. *Chest*, **122**, 2224–2229.
Metintas, M., Metintas, S., Ucgun, I., and Baykul, C. (2002b) *Eskisehir İli kırsal alanında çevresel asbest teması ile ilgili solunum sistemi sorunları*. TÜBİTAK Project No. YDABÇAG-585.
Metintas, M., Metintas, S., Ak, G., Erginel, S., Alatas, F., Kurt, E., Ucgun, I., and Yildirim, H. (2008) Epidemiology of pleural mesothelioma in a population with non-occupational asbestos exposure. *Respirology*, **13**, 117–121.
Metintaş, S., Batırel, H.F., Bayram, H. Yılmaz, Ü., Karadağ, M., Ak, G., and Metintas, M., (2017) Turkey national mesothelioma surveillance and environmental asbestos exposure control program. *International Journal of Environmental Research and Public Health*, **14**, doi: 10.3390/ijerph14111293.
Mével, C. (2003) Serpentinization of abyssal peridotites at mid-ocean ridges. *Comptes Rendus Geoscience*, **335**, 825–852.
Montes-Hernandez, G., Renard, F., Chiriac, R., Findling, N., and Toche, F. (2012) Rapid precipitation of magnesite micro-crystals from $Mg(OH)_2$-H_2O-CO_2 slurry enhanced by NaOH and a heat-ageing step (from 20 to 90ºC). *Crystal Growth and Design*, **12**, 5233–5240.
Moody, J.B. (1976) Serpentinization: A review. *Lithos*, **9**, 125–138.
Moore, D.M. and Reynolds, R.C., Jr. (1989) *X-ray Diffraction and the Identification and Analysis of Clay Minerals*. Oxford University Press, New York, 332 pp.
MTA (2002) 1/500,000 scale geological map of Turkey – Zonguldak, Sinop, Kayseri, Ankara, General Directorate of Mineral Research and Exploration of Turkey.
Mumpton, F.A. and Thompton, C.S. (1975) Mineralogy and origin of the Coalinga asbestos deposit. *Clays and Clay Minerals*, **23**, 131–144.
Niu, Y. (2004) Bulk-rock major and trace element compositions of abyssal peridotites: Implications for mantle melting, melt extraction and post-melting processes beneath mid-ocean ridges. *Journal of Petrology*, **45**, 2423–2458.
Nuriel, P., Katzir, Y., Abelson, M., Valley, J.W., Matthews, A., Spicuzza, M.J., and Ayalon, A. (2009) Fault-related oceanic serpentinization in the Troodos ophiolite, Cyprus: Implications for a fossil oceanic core complex. *Earth and Planetary Science Letters*, **282**, 34–46.
O'Hanley, D.S. (1996) *Serpentinites: Records of Tectonic and Petrological History*. Oxford University Press, New York, 277 p.
Okay, A.I. and Tüysüz, O. (1999) Tethyan sutures of northern Turkey. Pp. 475–515 in: *The Mediterranean Basins: Tertiary Extension Within the Alpine Orogen* (B. Durand, L. Jolivet, F. Horváth, and M. Séranne, editors). Geological Society, London, Special Publications, 156.
Pacella, A., Andreozzi, G.B., and Fournier, J. (2010) Detailed crystal chemistry and iron topochemistry of asbestos occurring in its natural setting: A first step to understanding its chemical reactivity. *Chemical Geology*, **277**, 197–206.
Page, N.J. (1968) Chemical differences among the serpentine polymorphs. *American Mineralogist*, **53**, 201–215.
Paulick, H., Bach, W., Godard, M., De Hoog, J.C.M., Suhr, G., and Harvey, J. (2006) Geochemistry of abyssal peridotites (Mid-Atlantic Ridge, 15º20′N, ODP Leg 209): Implications for fluid/rock interaction in slow spreading environments. *Chemical Geology*, **234**, 179–210.
Rojay, B. (2013) Tectonic evolution of the Cretaceous Ankara Ophiolitic Mélange during the Late Cretaceous to pre-Miocene interval in Central Anatolia, Turkey. *Journal of Geodynamics*, **65**, 66–81.
Ross, M. and Nolan, R.P. (2003) History of asbestos discovery and use and asbestos-related disease in context with the occurrence of asbestos within ophiolite complexes. Pp. 447–470 in: *Ophiolite Concept and the Evolution of Geological Thought: Boulder, Colorado* (Y. Dilek and S. Newcomb, editors). Geological Society of America Special Paper, 373.
Saccocia, P.J., Seewald J.S., and Shanks III W.C. (2009) Oxygen and hydrogen isotope fractionation in serpentine–-water and talc–water systems from 250 to 450ºC, 50 MPa. *Geochimica et Cosmochimica Acta*, **73**, 6789–6804.
Sarıfakıoğlu, E., Sevin, M., Esirtgen, E., Bilgiç, T., Duran, S., Parlak, O., Karabalık, N., Alemdar, S., Dilek, Y., and Uysal, I. (2011) *The Geology of Ophiolitic Rocks around Çankırı-Çorum Basin: Petrogenesis, Tectonics and Ore Deposits: Ankara, Turkey*. General Directorate of Mineral Research and Exploration (MTA) Report 11449, 196 p.
Sarıfakıoğlu, E., Dilek, Y., and Sevin, M. (2014) Jurassic–Paleogene intra-oceanic magmatic evolution of the Ankara mélange, north-central Anatolia, Turkey. *Solid Earth*, **5**, 77–108.
Sarıfakıoğlu, E., Dilek, Y., and Sevin, M. (2017) New synthesis of the Izmir-Ankara-Erzincan suture zone and the Ankara mélange in northern Anatolia based on new geochemical and geochronological constraints, in: *Tectonic Evolution, Collision, and Seismicity of Southwest Asia: In Honor of Manuel Berberian's Forty-Five Years of Research Contributions* (R., Sorkhabi, editor). Geological Society of America Special Paper 525.
Savin, S.M. and Epstein, S. (1970) The oxygen and hydrogen isotope geochemistry of clay minerals. *Geochimica et Cosmochimica Acta*, **34**, 25–42.
Sevin, M. and Uğuz, M.F. (2011) *Geological Map of Çankırı G 30 Quadrangle, Scale 1:100.000*, General Directorate of Mineral Research and Exploration (MTA) Publications, Ankara, Turkey.
Sheppard, S.M.F. and Gilg, H.A. (1996) Stable isotope geochemistry of clay minerals. *Clay Minerals*, **31**, 1–24.
Sheppard, S.M.F., Nielsen, R.L., and Taylor, H.P. (1969) Oxygen and hydrogen isotope ratios of clay minerals from porphyry copper deposits. *Economic Geology*, **64**, 755–777.
Sonzogni, Y., Treiman, A.H., and Schwenzer, S.P. (2017) Serpentinite with and without brucite: A reaction pathway analysis of a natural serpentinite in the Josephine ophiolite, California. *Journal of Mineralogical and Petrological Sciences*, **112**, 59–76.
Sun, S.-s. and McDonough, W.F. (1989) Chemical and isotopic systematics of oceanic basalts: Implications for mantle composition and processes. Pp. 313–345 in: *Magmatism in the Ocean Basins* (A.D. Saunders and M.J. Norry, editors). Geological Society, London, **42**.
Şengör, A.M.C. and Yılmaz, Y. (1981) Tethyan evolution of Turkey: A plate tectonic approach. *Tectonophysics*, **75**, 181–241.
Turkish Mesothelioma Working Group (2015) Turkey asbestos control strategic plan final report. *Turkish Thoracic Journal*, **16**, S1–S26.
Üner, T. and Çakır, Ü. (2011) Mineralogical, petrographical and geochemical characteristics of Eldivan Ophiolite (Çankırı) harzburgitic tectonites. *Mineral Research and Exploration Bulletin*, **143**, 75–94.
Van Gosen, B.S. (2007) The geology of asbestos in the United States and its practical applications. *Environmental and Engineering Geoscience*, **XIII**, 55–68.
Wenner, D.B. and Taylor, H.P. (1973) Oxygen and hydrogen isotopic studies of the serpentinization of the ultramafic rocks in oceanic environments and continental ophiolitic complexes. *American Journal of Science*, **273**, 207–239.
Whitney, D.L. and Evans, B.W. (2010) Abbreviations for names of rock-forming minerals. *American Mineralogist*, **95**, 185–187.
Wicks, F.J. and Whittaker, E.J.W. (1977) Serpentine textures

and serpentinization. *Canadian Mineralogist*, **15**, 459–488.
Yılmaz, Y., Genç, S.C., Gürer, F., Bozcu, M., Yılmaz, K., Karacık, Z., Altunkaynak, S., and Elmas, A. (2000) When did the western Anatolian grabens begin to develop? Pp. 353–384 in: *Tectonics and Magmatism in Turkey and the Surrounding Area* (E. Bozkurt, J.A. Winchester, and J.D.A. Piper, editors). Special Publications, 173, Geological Society of London.
Zaremba, T., Krzakała, A., Piotrowski, J., and Garczorz, D. (2010) Study on the thermal decomposition of chrysotile asbestos. *Journal of Thermal Analysis and Calorimetry*, **101**, 479–485.
Zheng Y.-F. (1993) Calculation of oxygen isotope fractionation in hydroxyl-bearing silicates. *Earth and Planetary Science Letters*, **120**, 247–263.

(*Received 2 November 2017; revised 19 February 2018; Ms. 1234; AE: W. Huff*)